Asymptotic and Numerical Algorithms in Applied Electromagnetism

by

Le Wang

A Dissertation Presented in Partial Fulfillment
of the Requirements for the Degree
Doctor of Philosophy

Approved November 2012 by the
Graduate Supervisory Committee:

George Pan, Chair
Hongyu Yu
James Aberle
Rodolfo Diaz
Jennifer Kitchen

ARIZONA STATE UNIVERSITY

December 2012

ABSTRACT

Asymptotic and Numerical methods are popular in applied electromagnetism. In this work, the two methods are applied for collimated antennas and calibration targets, respectively.

As an asymptotic method, the diffracted Gaussian beam approach (DGBA) is developed for design and simulation of collimated multi-reflector antenna systems, based upon Huygens principle and independent Gaussian beam expansion, referred to as the frames. To simulate a reflector antenna in hundreds to thousands of wavelength, it requires $10^7 – 10^9$ independent Gaussian beams. To this end, high performance parallel computing is implemented, based on Message Passing Interface (MPI).

The second part of the dissertation includes the plane wave scattering from a target consisting of doubly periodic array of sharp conducting circular cones by the magnetic field integral equation (MFIE) via Coiflet based Galerkin's procedure in conjunction with the Floquet theorem. Owing to the orthogonally, compact support, continuity and smoothness of the Coiflets, well-conditioned impedance matrices are obtained. Majority of the matrix entries are obtained in the spectral domain by one-point quadrature with high precision. For the oscillatory entries, spatial domain computation is applied, bypassing the slow convergence of the spectral summation of the non-damping propagating modes. The simulation results are compared with the solutions from an RWG-MLFMA based commercial software, FEKO, and excellent agreement is observed.

To My Parents Shengcao Wang and Guojun He

ACKNOWLEDGMENTS

I would like to express my heartfelt gratitude to my advisor and committee chair, Professor George Pan, without whom my research and this dissertation would not have been possible. I am very grateful for his advising, encouragement, inspiration, and enduring patience. Dr. Pan gave me this opportunity to come to ASU to pursuit my Ph.D. in EE department. His help has changed my life trajectory and become my life-long heritage.

I would also like to give special appreciation to Dr. Yu, Dr. Aberle, Dr. Diaz, and Dr. Kitchen for serving as my committee members. I benefit a lot from the Antenna course by Dr. Diaz, RF courses by Dr. Aberle. Dr. Yu has also given me very valuable suggestions on RF MEMS fabrication.

TABLE OF CONTENTS

Page

CHAPTER Page

APPENDIX Page

LIST OF TABLES

LIST OF FIGURES

Figure Page

Figure Page

CHAPTER 1

INTRODUCTION

1.1 Reflector antennas design

The diffracted Gaussian beam approach (DGBA) [1] for design and analysis of the multi-reflector antenna systems is presented in Chapter 2-5. This method has efficiency and modularity advantage compared to the time-consuming PO based methods and geometrical optics (GO) plus uniform theory of diffraction (UTD) or geometrical theory of diffraction (GTD) method.

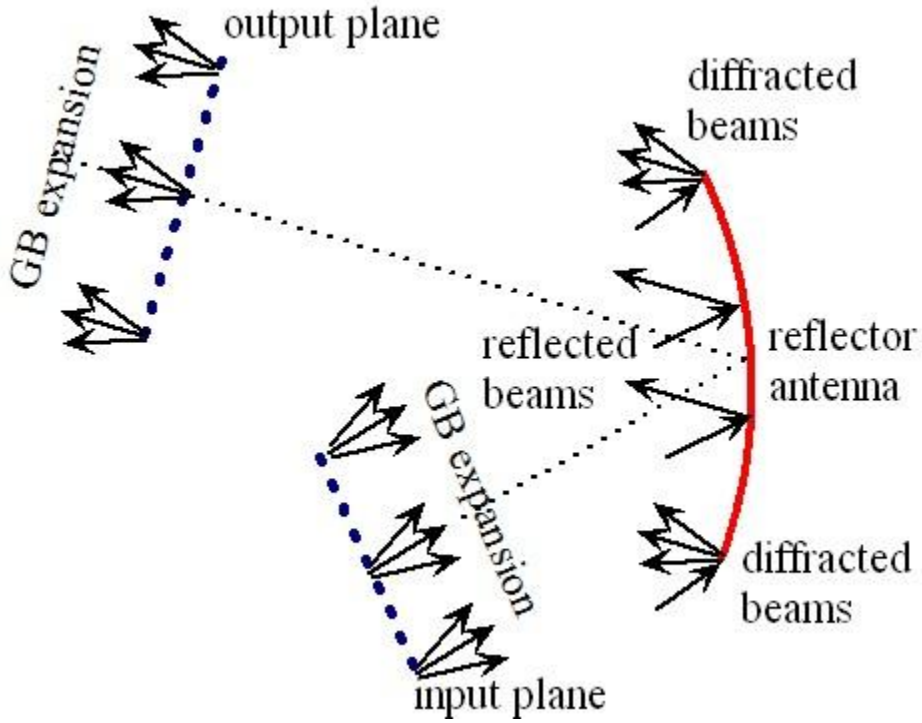

Fig. 1.1. A single step of the DGBA in a multi-reflector analysis.

Fig. 1.1 shows a single step in the DGBA multi-reflector analysis. The incident field on an input plane is expanded [2][3] in terms of fundamental 3-D

Gaussian beam modes. And each beam has a beam-width of several wavelengths. The elementary beams are propagated to the reflector to be analyzed. Reflection of these beams is treated in a geometrical optics manner [4] and diffraction is then treated by applying Boundary Diffraction Wave (BDW) method. Reflection of Gaussian beam will change the radii of wavefront curve surface which changes the parameter q of Gaussian beam. The BDW of Gaussian beam is approximately calculated by the steepest descent method [5][6][7][8]. The output beam is a superposition of all reflected and diffracted elementary beams and can again be expanded into a set of Gaussian beams. However when dealing reflectors in tens to hundreds wavelength, more than 10 million elementary Gaussian beams will be generated. Computation of reflection and diffraction of these Gaussian beams may cost tens or hundreds hours on ordinary PCs. In order to speed up computations, the parallel computation method for DGBA on clusters is developed. After expansion, all Gaussian beams are evenly distributed to the assigned CPUs. Upon reflection and diffraction of computation, the field on the selected output plane is evaluated by the summation of all coming different Gaussian beams. Simulation results on Saguaro cluster at Arizona State University are presented at the last part of this paper. The computation speed is highly accelerated as expected.

1.2 Scattering From a Doubly Periodic Surface

Microwave remote sensing [13] is often used for astronomical studies, military applications and environmental monitoring. The term used for characterizing the emission by the scene observed by the radiometer is the brightness temperature T_B, which may vary from zero Kelvin (for a non-emissivity medium) to a maximum value equal to the physical temperature T_0 of the scene (for a perfect emitter known as a blackbody). In other words, the emissivity $e\ (=T_B/T_0)$ varies between zero and unity.

Scattering by an infinite rough surface, such as land and ocean, is characterized by the bistatic scattering cross-section per unit area $\sigma^o(\theta_0, \phi_0; \theta_s, \phi_s; p_0, p_s)$ which relates the magnitude of the power scattered in the direction (θ_s, ϕ_s) with polarization p_s to the power incident upon the surface from the direction (θ_0, ϕ_0) with polarization p_0 (Fig. 1.2). σ^o is known as the surface scattering coefficient. p_0 and p_s could be *v* or *h*, which is vertically or horizontally polarized.

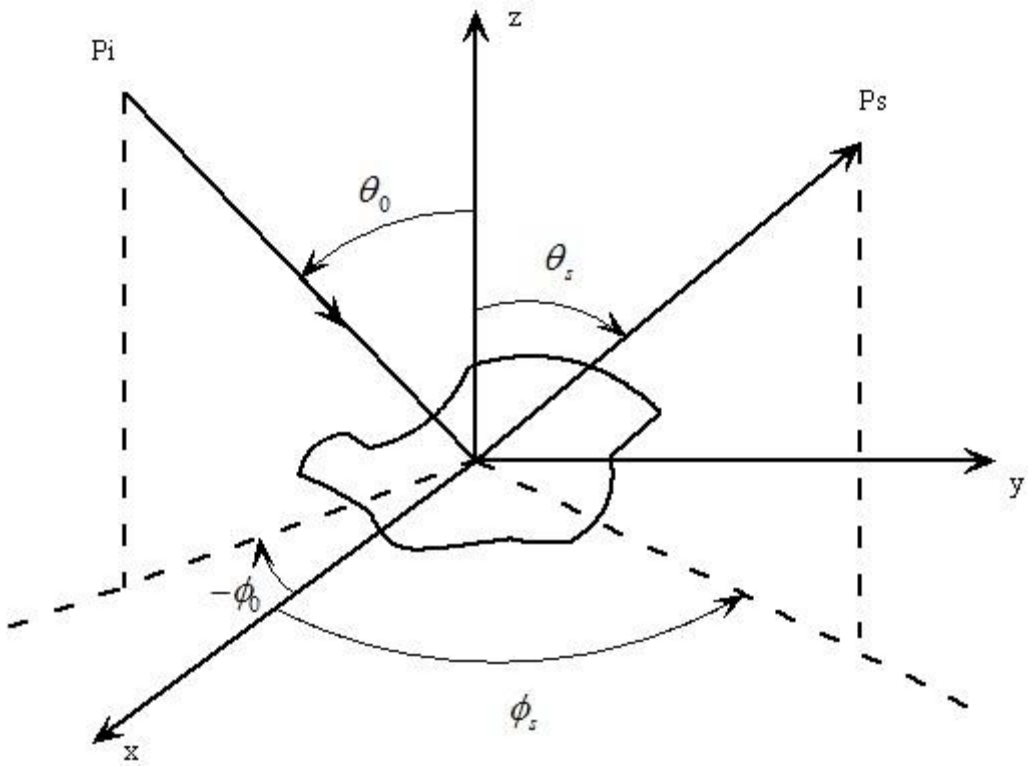

Fig. 1.2. Geometry of incident and scattered.

Peake (1959) developed expressions for the polarized emissivity $e(\theta_0, \phi_0; p_0)$ of a surface observed from the direction (θ_0, ϕ_0) and for the scattered temperature $T_{SC}(\theta_0, \phi_0; p_0)$ in terms of σ^o:

$$e(\theta_0,\phi_0;p_0) = 1 - \frac{1}{4\pi\cos\theta_0}\int\left[\sigma^o(\theta_0,\phi_0;\theta_s,\phi_s;p_0,p_0) + \sigma^o(\theta_0,\phi_0;\theta_s,\phi_s;p_0,p_s)\right]d\Omega_s \tag{1-1}$$

and

$$T_{SC}(\theta_0,\phi_0;p_0) = \frac{1}{4\pi\cos\theta_0}\int\left[\sigma^o(\theta_0,\phi_0;\theta_s,\phi_s;p_0,p_0) + \sigma^o(\theta_0,\phi_0;\theta_s,\phi_s;p_0,p_s)\right]T_{DN}(\theta_s,\phi_s)\,d\Omega_s \tag{1-2}$$

where T_{DN} is the downward-emitted atmospheric apparent temperature.

Special rough surface is often used as calibration in microwave remote sensing area. Before fabrication, the scattering property and emissivity of the calibration source must be predicted and calculated, which provide reference data for system calibration.

A sharp-cone array is a kind of rough surface for calibration. In Beijing Institute of Aeronautics, research people [15] build a cone array as indicated in Fig. 1.3

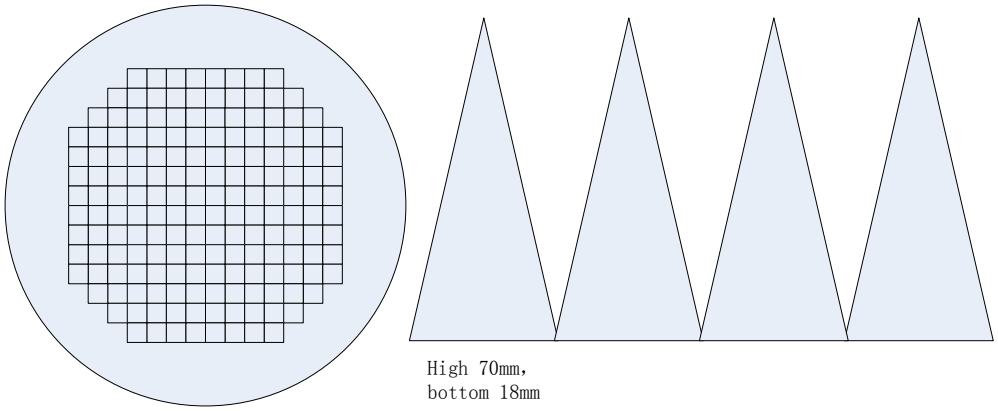

Fig. 1.3. Top view and side view of cone array.

There are 14 corns in diameter location, arranged in 8 rows. And the number decreases to 8 on the edge of each column (the reduction of two per line in equal difference).

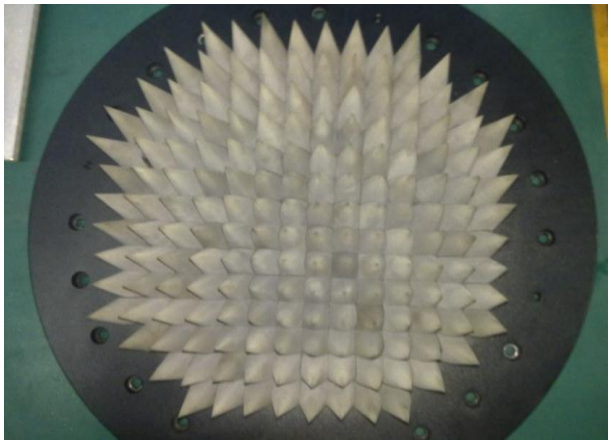

Fig. 1.4. Physical diagram of cone array.

Relevant frequency is from 10GHz to 100GHz. There material used to build this cone array includes metal, metal covered by a thin absorbing material and dielectric material. Calibration data for each case should be computed well.

The calibration sources have been studied by optical methods [14][15] and the finite difference time domain (FDTD) method [16][17]. Despite the versatility and simplicity of the FDTD, high precision results may be restricted owing to the stair case discretization and artificial boundaries of the FDTD. On the other hand, the open boundary nature of scattering and radiation problems preferably choose the integral equation method based method of moments (MoM) [18]. Nonetheless, such a scattering problem is electrically large. To alleviate high demanding of computation resources in terms of the CPU time and memory consumption, the Floquet theorem enforced periodic method of moments (PMM) were reported [19][21].

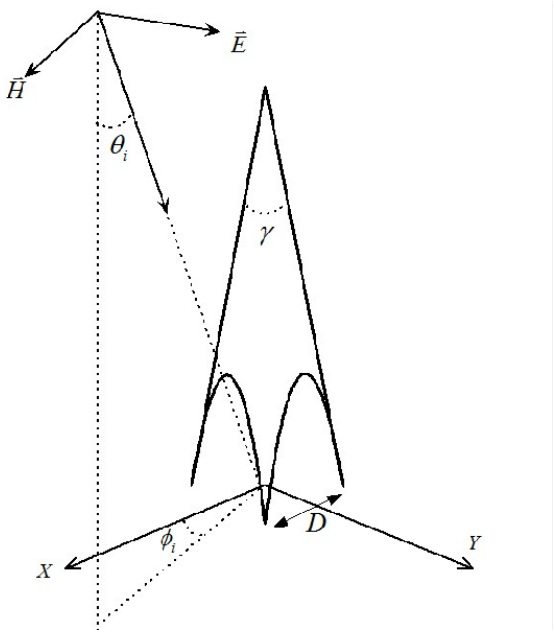

Fig. 1.5. One cone profile and incidence configuration.

In this dissertation, the MoM with the Floquet theorem are combined, assuming the array to be infinite and using a plane wave incident, so that only one period, namely a single cone in the array, is discretized. While the electric field integral equation (EFIE) was solved in [19][21], the magnetic field integral equation (MFIE) are solved because it is well-posted. As a result, there is no need to employ the RWG formulation, yet well-conditioned impedance matrix is guaranteed. In fact, the standard Cartesian coordinate system is used, even though the cone is very sharp, possessing discontinuities in the 1st spatial derivatives on the vertex and four legs as seen in Fig. 1.5. The Coiflets is employed as the basis and testing functions to conduct Galerkin's procedure. The Coiflets are

orthonormal, continuous, smooth, compact supported, and nearly symmetric with zero moment properties [22]. The smoothness of the Coiflet in spatial domain leads to rapid decay in the spectral domain, while zero moments correspond to minimum low frequency components in its spectrum. Hence, The Coifman wavelets are highly concentrated in the spatial and spectral domains, allowing much coarser mesh to achieve the high precision results of collocation method with very fine mesh, and demonstrating a memory saving in 39 fold [23]. To analyze plane wave scattering from a doubly periodically conic surface, a hybrid spectral and spatial domain formulation is conducted in CHAPTER 7, where the Coifman scalets (Coiflets) are employed to perform Galerkin's procedure in the PMM. In addition to the aforementioned merits of continuity, smoothness, orthogonality and nearly symmetry, the Coifman scalets of order L = 4 have three vanishing moments. This Dirac-δ like property provides high precision O(h5) one-point quadrature, reducing impedance matrix filling computation into O(n). Coiflets have been successfully implemented in rough random surface scattering [23]. However, due to boundary truncation in periodic problems, intervallic Coiflets [25][26] would be required to handle boundary truncations, which will complicate mathematics and destroy several important merits of the Coiflets. In order to avoid this loss, I split the unknown doubly periodically surface current

into four unknown currents, which are equal to zero at boundaries and maintain the double periodicity. Hence, I may utilize the standard Coiflets to attack periodic structures. When computing an impedance matrix entry in spectral domain, I sum up all propagating modes and sufficient numbers of evanescent modes. The attenuation factor $e^{-jk_z|z-z\prime|}$ in the Green's function plays an important role. For those entries representing the source and field points with different elevations, $z \neq z'$, the spectral domain summation converges very fast, namely, just a few propagating modes may provide accurate value of the entry. Whereas for entries with z = z′ , especially for self-entries, the attenuation factor vanishes. Thus, the summation converges slowly and one needs a lot of undamped propagating modes to reach the precision. In this situation, spatial domain computation is applied since it is faster than the spectral domain computation. Once the matrix equation has solved and the induced surface current on the reference cone is obtained, I may conduct the far field calculations. By the Floquet theorem, the surface current on each cone in an infinite array is identical, subject to a phase shift. The current distribution on a finite sized array is obtained as if each cone were among an infinite array. This current distribution is then used to produce the far-zone fields and radar cross sections (RCS). If the array is large enough, the edge effect from the truncation should be relatively small. I present

the Bi-static RCS results of a 9×9 conic array and compare with the solution from the commercial software, FEKO in CHAPTER 8.

CHAPTER 2

GAUSSIAN BEAM EXPANSION

2.1 Aperture expansion theory

In this chapter, the classical aperture theory, i.e. the methodology of determining the electromagnetic field in the half-space z>0 given the appropriate aperture field distribution at z=0, is presented. In 3D application, there are two transverse electric field E_x and E_y on a plane z = 0 which are needed to expand the field in terms of circular Gaussian beams. Generalizing the expansion to a 2-D signal results in an expansion of the form [2], there is

$$f(x,y) = \sum_{m,n,u,v} A_{mnuv} w_{2-D}(x - md_0, y - ud_0) \exp\left(j\left(n\Omega_0 x + v\Omega_0 y\right)\right) \quad (2\text{-}1)$$

with a Gaussian shaped window function

$$w_{2-D}(x,y) = \frac{\sqrt{2}}{L} \exp\left(-\pi\left(x^2 + y^2\right)/L^2\right) = w(x)w(y) \quad (2\text{-}2)$$

where f stands for either of the two transverse field components, L is the radius of the circular Gaussian beam and A_{mnuv} is the expansion coefficient, and d_0 represents the spatial shift and Ω_0 represents the spectral shift. The product $\Omega_0 d_0$ has to be chosen smaller than 2π (Gabor's representation) to ensure stability. The smaller it is compared to 2π, the smoother the shape of the dual frame function, it then resembling more and more the Gaussian shape of the window function. However the smaller the product is, the more Gaussian beams will be produced

which will burden the computation. Since the window function can be separated into the two transverse co-ordinates, so the 2-D dual frame function $\tilde{w}_{2-D}(x,y)$ can also be written as the product of two 1-D dual frame functions. The expansion coefficients are then calculated as

$$A_{mnuv} = \iint f(x,y)\tilde{w}(x-md_0)\tilde{w}(y-ud_0)\exp\left(-j\left(n\Omega_0 x + v\Omega_0 y\right)\right)dxdy \quad (2\text{-}3)$$

where $\tilde{w}$ is the dual frame function. Two-dimensional FFT can be utilized to find expansion coefficients with high numerical efficiency.

To describe the scalar field components E_x and E_y of each contributing term in the expansion everywhere in the half space $z \geq 0$, asymptotic techniques are employed. For the Gaussian shape of the window function, they will produce many complex beams source which are paraxially approximately equivalent to Gaussian beams. Let $B_{mnuv}(x, y, z)$ denote the beam mode corresponding to the expansion coefficient A_{mnuv} in (1.1) such that [3]

$$f(x,y,z) = \sum_{m,n,u,v}\left[A_{mnuv}\exp\left(j\left(mn+uv\right)\Omega_0 d_0\right)\right]B_{mnuv}(x,y,z); \quad z \geq 0 \quad (2\text{-}4)$$

Asymptotically derived to

$$B_{mnuv}(\rho_t, z_t) \cong \frac{\sqrt{2}}{L}\frac{q_{nv}(0)}{q_{nv}(z_t)}\exp\left(jk_0\left(z_t + \frac{\rho_t^2}{2q_{nv}(z_t)}\right)\right) \quad (2\text{-}5)$$

The transformed coordinates ρ_t and z_t are linked with the Cartesian co-ordinates x, y, z and the spectral components of the wave vector by the transformation

$$z_t = \left[n\Omega_0 \left(x - md_0 \right) + v\Omega_0 \left(y - ud_0 \right) + \sqrt{k_0^2 - \left(n\Omega_0 \right)^2 - \left(v\Omega_0 \right)^2} z \right] / k_0$$

$$k_0 = 2\pi / \lambda \tag{2-6}$$

$$\rho_t^{\,2} = \left(x - md_0 \right)^2 + \left(y - ud_0 \right)^2 + z^2 - z_t^2$$

z_t can be viewed as the projection of the vector pointing from the source point (mL_0, uL_0, 0) to the observation point (x, y, z) onto the direction

$$\hat{z}_t = \frac{1}{k_0} \left(n\Omega_0, v\Omega_0, \sqrt{k_0^2 - \left(n\Omega_0 \right)^2 - \left(v\Omega_0 \right)^2} \right) \tag{2-7}$$

of the wave vector. The complex beam parameter $q_{nv}(z_t)$ absorbs all the information about the local spot size $\omega(z_t)$ and the local radius of curvature $R(z_t)$ of the beam at each axial position z_t:

$$q_{nv}\left(z_t \right) = \left(\frac{1}{R\left(z_t \right)} + j \frac{\lambda}{\pi \omega^2 \left(z_t \right)} \right)^{-1} = z_t - j \frac{L^2}{\lambda} \left(1 - \left(\frac{n\Omega_0}{k_0} \right)^2 - \left(\frac{v\Omega_0}{k_0} \right)^2 \right) \tag{2-8}$$

The asymptotic expression (2-5) in terms of a complex beam is accurate only within the range of the paraxial approximation. Fig. 2.1 illustrates this interpretation of the expansion in terms of Gaussian beam modes. A number of spectral Gaussian beam modes located at each spatial 'sampling point' separated by d_0 with different directions.

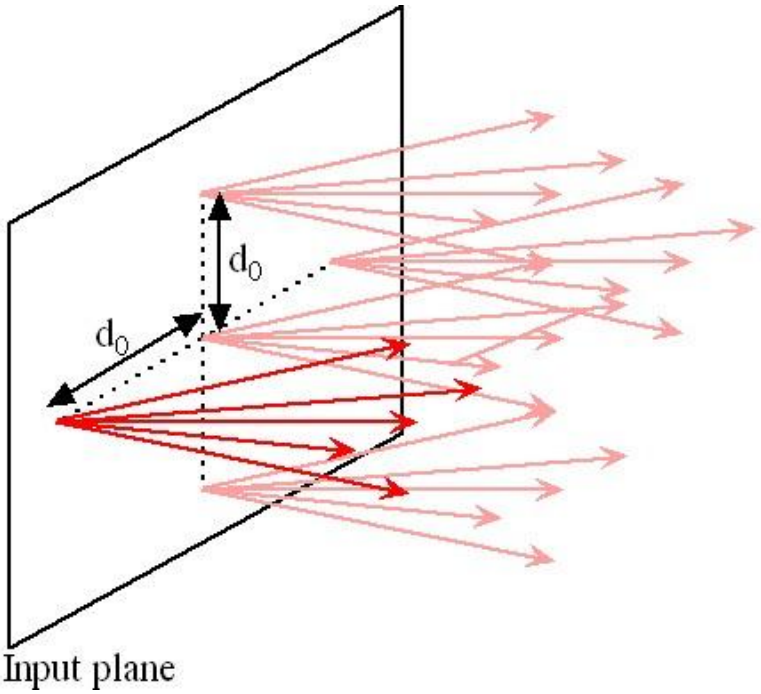

Fig. 2.1. Interpretation of the expansion in terms of Gaussian beam modes.

2.2 Gaussian beam expansion Example

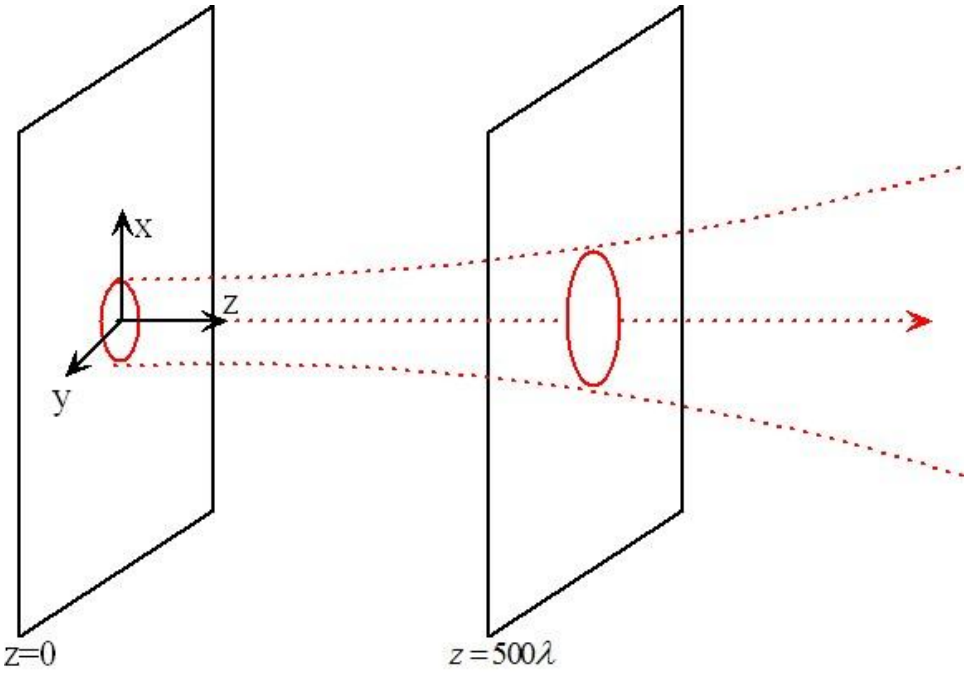

Fig. 2.2. Gaussian beam expansion example.

In Fig. 2.2 the example is illustrated. A Gaussian beam propagates in z direction from z=0 plane. I calculate electrical field Ey on z=500λ plane according to field Ey z=0 plane. The source plane is 40λ×40λ and expanded with d_0=2λ, L=8λ.

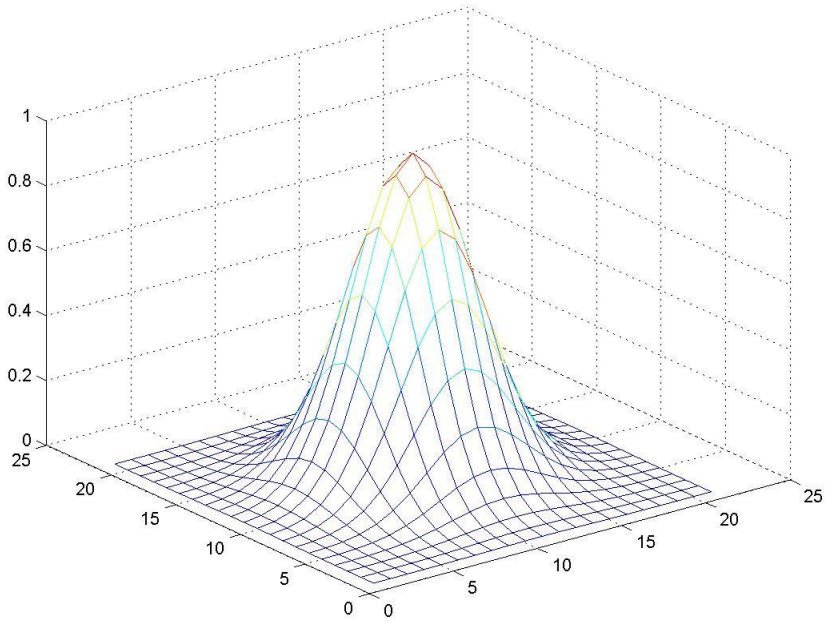

Fig. 2.3. Ey on z=0 plane (the plane is 40λ*40λ, sampling shift is 2λ).

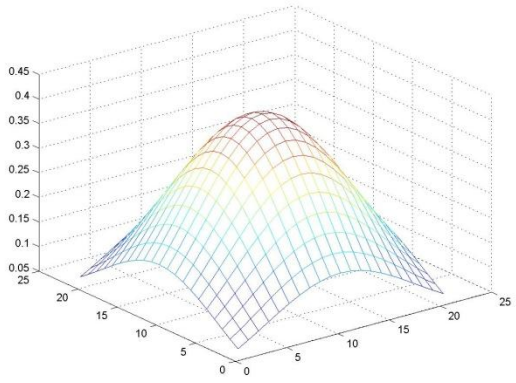

(a)

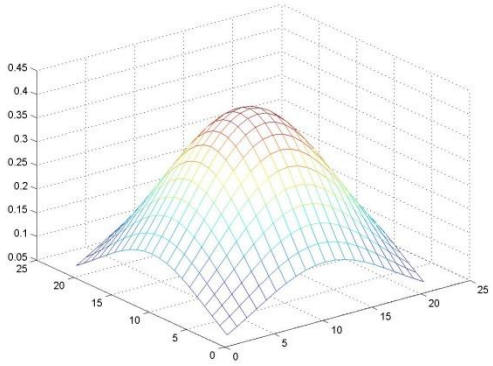

(b)

Fig. 2.4. Ey on z=500λ plane.

(a) is analytical solution and (b) is result from Gaussian beam expansion theory.

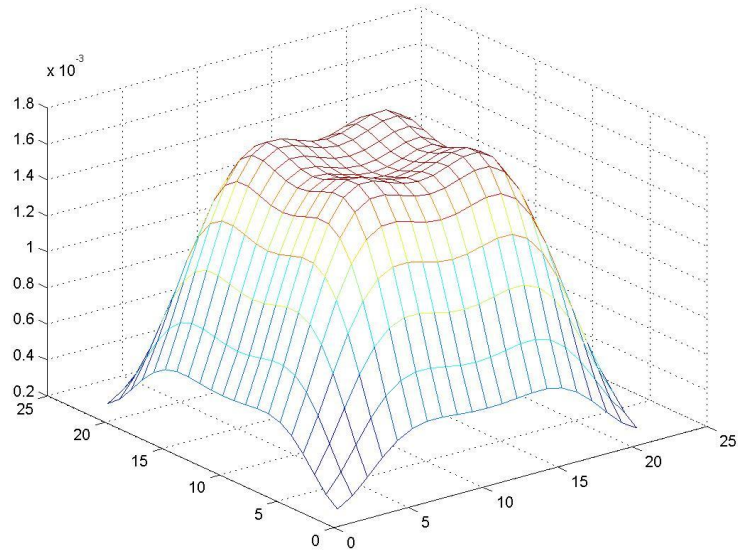

Fig. 2.5. Amplitude difference between analytical solution and Gaussian beam expansion theory.

The result indicates the deviation of Gaussian beam expansion method is less than 2/1000, when $d_0=2\lambda$, $L=8\lambda$. So 2λ sampling shift is acceptable considering the phase change on the plane which is perpendicular to propagation is not big. Of course smaller the sampling shift d_0, better the result will be. As for Gaussian beam width L, L/d_0 can not be very small, otherwise the result will not be good enough.

CHAPTER 3

GAUSSIAN BEAM REFLECTION

3.1 Properties of Rays in Uniform Region

The rays that are near to a given axial ray are called paraxial and are said to form a pencil. The rays of the pencil are normal to wavefronts. In the near area of the axial ray Oz, the wavefront through point O can be represented by the second-degree equation [4].

$$z = -\frac{1}{2}\vec{\rho}\cdot Q\vec{\rho} \tag{3-1}$$

Where $\vec{\rho} = \begin{bmatrix} x \\ y \end{bmatrix}$ is the transverse position vector represented by its components (x, y) with respect to the two principal directions of wavefront curvature $\hat{x}$ and $\hat{y}$.

$$Q = \begin{bmatrix} 1/R_1 & 0 \\ 0 & 1/R_2 \end{bmatrix} \tag{3-2}$$

Where R_1 and R_2 are the two principal radii of the curvature.

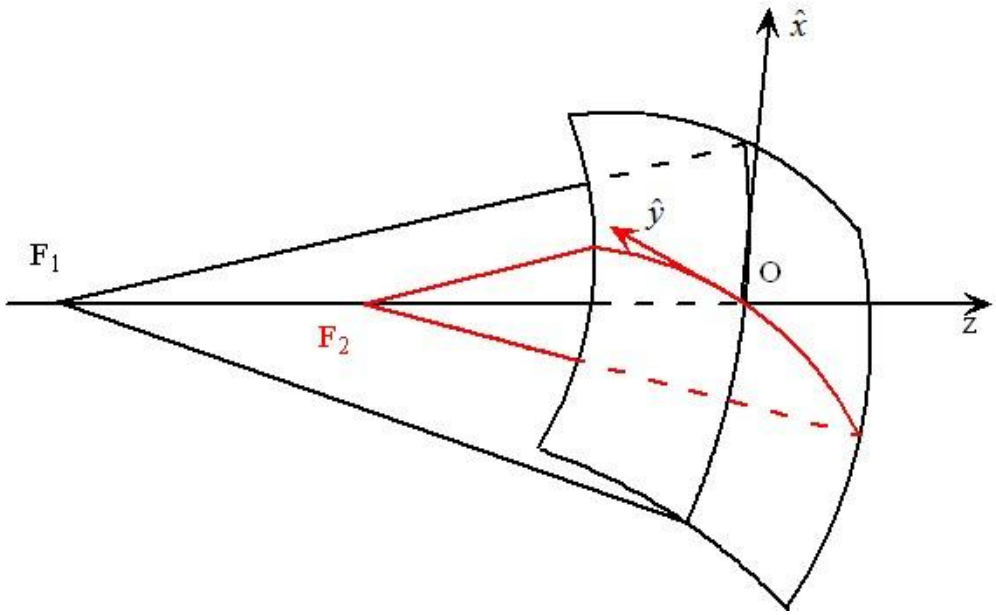

Fig. 3.1. Wavefront for a pencil with axis Oz.

How Q changes, or R_1 and R_2 change, under reflection through a curved surface Σ is needed to be found. A principle of phase matching will be used which is a direct consequence of Snell's law: the phase in the reflected pencil, at every point of the surface Σ, is the same as that in the incident pencil. Actually, the phase should be 180 degree difference. But it is simplified to the same in Q derivation. Let us take the origin O where the axis Oz of the incident pencil meets the surface Σ (Fig. 3.2). The normal $\hat{n}$ to the surface makes angle θ with Oz. Let's set the reference to be $\hat{x}_1, \hat{y}_1$ which are orthonormal vectors perpendicular to $\hat{n}$. Then the equation of the surface Σ near O, should be written as

$$\vec{r}(\vec{t}) = \vec{t} - \frac{1}{2}(\vec{t} \cdot C\vec{t})\hat{n} \qquad (3\text{-}3)$$

Where $\vec{t} = t_1\hat{x}_1 + t_2\hat{y}_1$ and C is a 2×2 matrix which defines the curvature of Σ. The phase in the incident pencil is kS(r) with

$$S(\vec{r}) = z + \frac{1}{2}\vec{\rho} \cdot Q\vec{\rho} \tag{3-4}$$

The coordinates $(\vec{\rho}, z)$ of $\vec{r}(\vec{t})$ are

$$\begin{aligned} \vec{\rho} &= \Theta\vec{t} + O(t^2) \\ z &= \vec{v} \cdot \vec{t} - \frac{1}{2}\vec{t} \cdot C\vec{t}\ \cos\theta + O(t^2) \end{aligned} \tag{3-5}$$

where Θ is the matrix that expresses the projection of the vector $\vec{t}$ on the plane z =0, and $\vec{v} = v_1\hat{x}_1 + v_2\hat{y}_1$ is the projection of $\hat{z}$ on the plane L tangent to Σ . The components of $\vec{v}$ are $v_1=\hat{x}_1 \cdot \hat{z}$, $v_2=\hat{y}_1 \cdot \hat{z}$. If the reference vectors are chose such that $\hat{y} = \hat{y}_1$ is perpendicular to zOw and $\hat{x}_1$, $\hat{x}$ are in the plane zOw making the angle θ between them (Fig. 3.2), the matrix Θ is

$$\Theta = \begin{bmatrix} \cos\theta & 0 \\ 0 & 1 \end{bmatrix} \tag{3-6}$$

If the reference vectors are not in this special configuration, they can be derived by a simple change of coordinate; alternatively, the projection operator Θ could be evaluated directly

$$\Theta = \begin{bmatrix} \hat{x} \cdot \hat{x}_1 & \hat{x} \cdot \hat{y}_1 \\ \hat{y} \cdot \hat{x}_1 & \hat{y} \cdot \hat{y}_1 \end{bmatrix} \tag{3-7}$$

Substituting Equation (3-5) in the expression Equation (3-4) for S(r) leads to

$$S(\vec{r}) = \vec{v} \cdot \vec{t} + \frac{1}{2}\vec{t} \cdot \Gamma\vec{t} \tag{3-8}$$

Where

$$\Gamma = \Theta^T Q \Theta - C\cos\theta \tag{3-9}$$

The phase is the sum of a linear terms $k\vec{v}\cdot\vec{t} = \vec{\kappa}\cdot\vec{t}$, where $\vec{\kappa}$ is the projection on the tangent plane L of the axial wave vector $k_0 z$, and a quadratic term defined by the 2 x 2 symmetric matrix Γ.

Consider now the reflected pencil described with the same letter as the incident one, by being primed. The phases are matched if both linear and quadratic terms coincide. This means that

$$\begin{aligned} \vec{\kappa}' &= \vec{\kappa} \\ k'\Gamma' &= k\Gamma \end{aligned} \tag{3-10}$$

The first condition means the incident angle is equal to the reflected angle. The second indicates how the curvature is transformed

$$k'\left(\Theta'^T Q'\Theta' - C\cos\theta'\right) = k\left(\Theta^T Q\Theta - C\cos\theta\right)$$

or (3-11)

$$k'\Theta'^T Q'\Theta' = k\Theta^T Q\Theta + hC$$

The contribution of the surface curvature C is multiplied by $h = k'\cos\theta' - k\cos\theta$, which is the variation of the wave vector when reflected by the surface Σ.

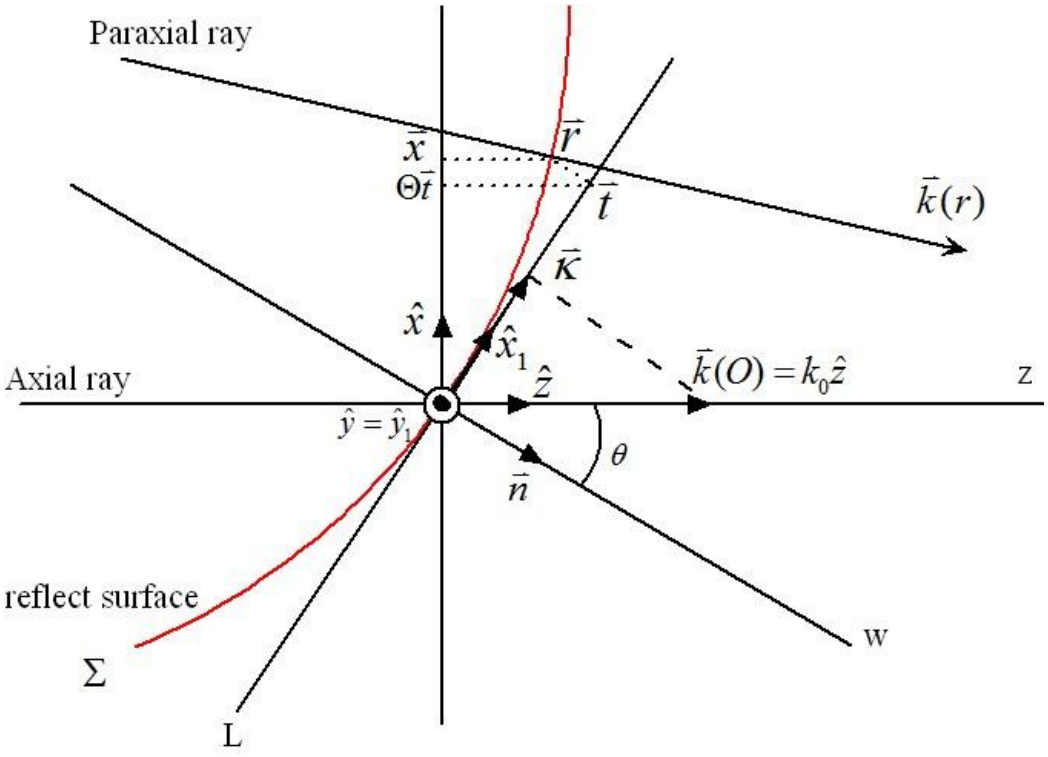

Fig. 3.2. Reflection axes.

3.2 Parameters change of Gaussian beam reflection

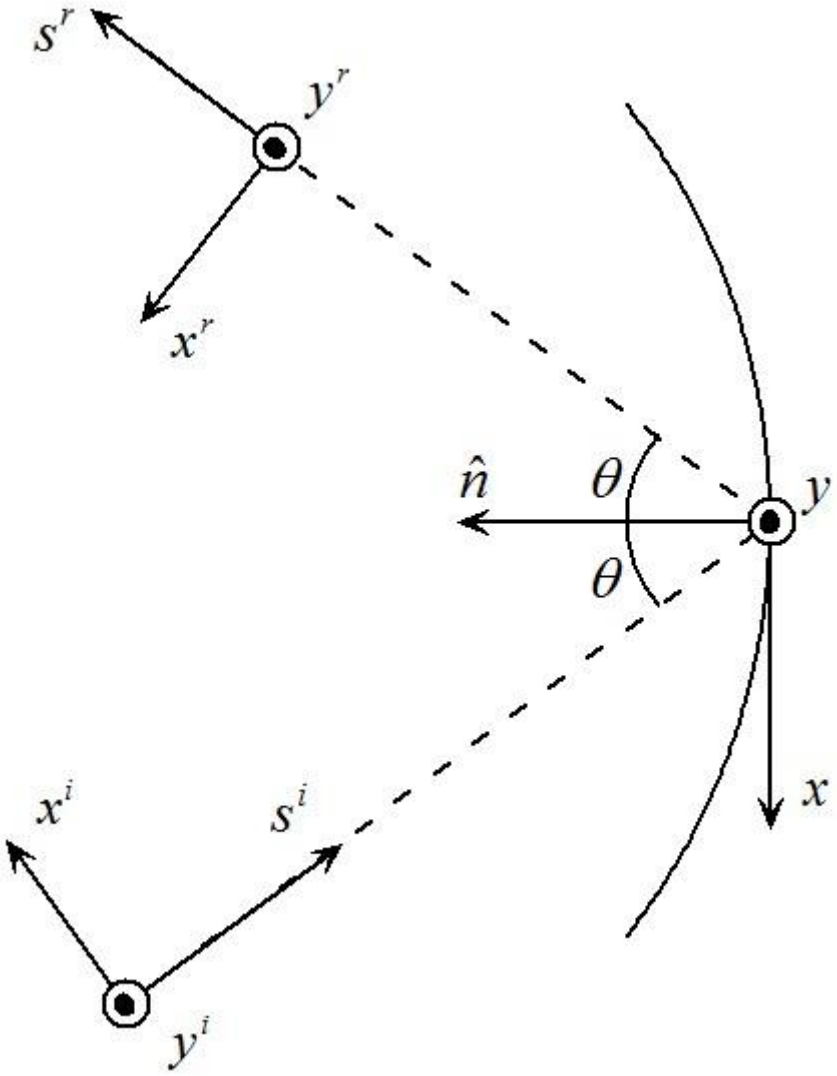

Fig. 3.3. Local coordinates of Gaussian beam reflection.

For one Gaussian beam reflection, it is convenient to do all calculations in the ray-based coordinate system $\left(\hat{\mathrm{x}}^{\mathrm{i,c,r}}, \hat{\mathrm{y}}^{\mathrm{i,c,r}}\right)$ as illustrated in Fig. 3.3. The two principal directions of curvature of surface $\left(\mathrm{u}^{\mathrm{i,c,r}}, \mathrm{v}^{\mathrm{i,c,r}}\right)$ are transformed as:

$$\begin{pmatrix} u^{i,c,r} \\ v^{i,c,r} \end{pmatrix} = \begin{bmatrix} \cos\left(\alpha_{i,c,r}\right) & \sin\left(\alpha_{i,c,r}\right) \\ -\sin\left(\alpha_{i,c,r}\right) & \cos\left(\alpha_{i,c,r}\right) \end{bmatrix} \begin{pmatrix} x^{i,c,r} \\ y^{i,c,r} \end{pmatrix} \tag{3-12}$$

The rotation angle $\alpha_{i,c,r}$ is the angle between $\hat{x}^{i,c,r}$ and the first principal direction of curvature of surface.

And the direction of the reflected ray, using Snell's law is

$$\hat{s}^r = \hat{s}^i + 2\cos(\theta)\hat{n} \tag{3-13}$$

Substituting Equation (3-12) to (3-11) leads to

$$\begin{pmatrix} \Sigma_r \\ \cos(2\alpha_r)\Delta_r \\ \sin(2\alpha_r)\Delta_r \end{pmatrix} =$$

$$\begin{pmatrix} \Sigma_i \\ \cos(2\alpha_i)\Delta_i \\ -\sin(2\alpha_i)\Delta_i \end{pmatrix} + \begin{bmatrix} \frac{1}{\cos\theta}+\cos\theta & \frac{1}{\cos\theta}-\cos\theta & 0 \\ \frac{1}{\cos\theta}-\cos\theta & \frac{1}{\cos\theta}+\cos\theta & 0 \\ 0 & 0 & 2 \end{bmatrix} \times \begin{pmatrix} \Sigma_c \\ \cos(2\alpha_c)\Delta_c \\ \sin(2\alpha_c)\Delta_c \end{pmatrix} \tag{3-14}$$

With

$$\Sigma_{i,c,r} = \left(1/R_2^{i,c,r} + 1/R_1^{i,c,r}\right)/2 \quad \text{and} \quad \Delta_{i,c,r} = \left(1/R_2^{i,c,r} - 1/R_1^{i,c,r}\right)/2$$

The reflected beam is approximated by a circular beam with a complex beam parameter

$$q = \left(\frac{1}{\sqrt{R_1^r R_2^r}} + j\frac{\lambda}{\pi w^2}\right)^{-1} \tag{3-15}$$

At the reflection point, the spot size of the beam stays the same. So using the spot size and new q, the image Gaussian beam can be determined.

$$R(z) = z\left[1+(b/2z)^2\right] \quad \text{and} \quad w^2(z) = w_0^2\left[1+(2z/b)^2\right] \tag{3-16}$$

$$\text{Where} \quad b = kw_0^2$$

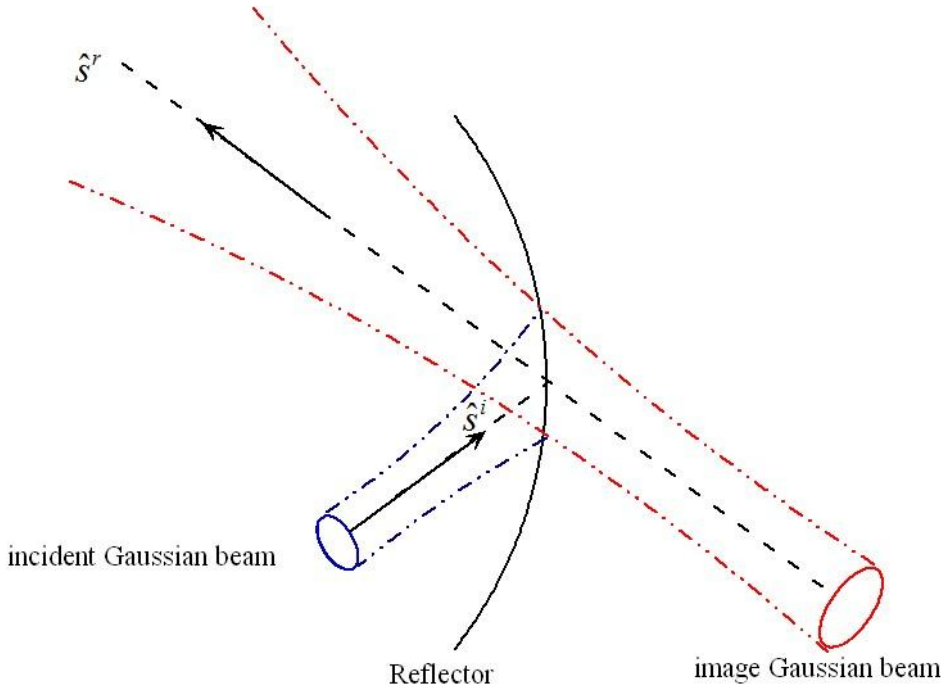

Fig. 3.4. Incident and image Gaussian beam.

As for the polarization of reflected beam, I separate incident E field to perpendicular and parallel parts as indicated in Fig. 3.5. According to the reflected beam polarization in Fig. 3.5, the dyadic reflection coefficient is

$$\bar{R} = \begin{bmatrix} -1 & 0 \\ 0 & -1 \end{bmatrix} \tag{3-17}$$

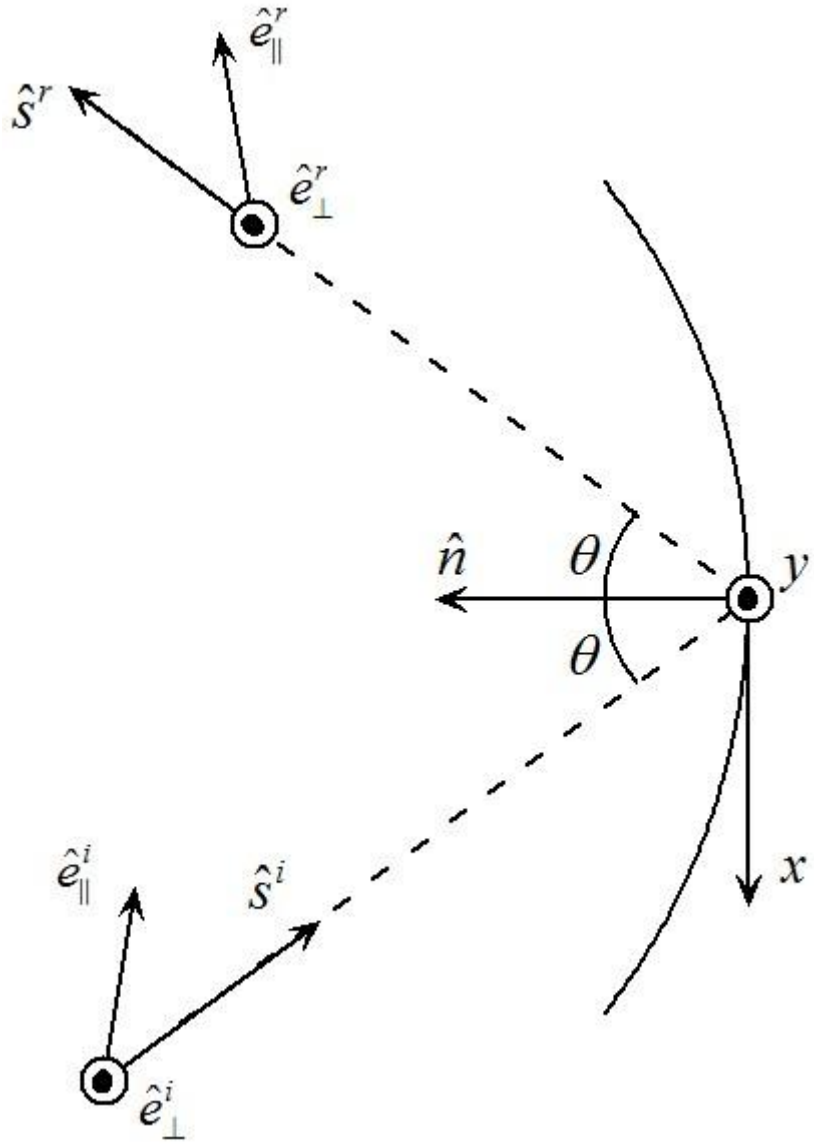

Fig. 3.5. Polarization of the incident and reflected beams.

CHAPTER 4

GAUSSIAN BEAM DIFFRACTION

4.1 Generalization of Boundary Diffraction Wave

Theoretical studies of diffraction of light by an obstacle whose dimensions are large compared to the wavelength are almost based on the classical principle of Huygens and Fresnel. According to this principle, each point of the unobstructed part of a primary wave is assumed to be a source of sphere waves and the diffracted field is considered to arise from the superposition of these sphere waves.

A different physical model for diffraction was suggested by Young in 1802 prior to the principle of Huygens and Fresnel. Young believed that the incident light undergoes a kind of reflection at the boundary of the diffracting body and he considered diffraction to arise from the interference between the direct light and the light propagated from each point of the boundary. But due to the early success of Fresnel's Theory and also due to no accurate analytical expression for Young's ideas, Fresnel's theory soon dominated in diffraction research and Young's explanation of diffraction has been forgotten by most people.

However after a long time, more and more evidence and experiments suggest that Young's theory is a good physical model which is probably more fundamental and simpler than principle of Huygens and Fresnel.

In 1962, Kenro Miyamoto and Emil Wolf [5][6] first proposed Boundary Diffraction Wave equation according to Helmholtz-Kirchholf integral equation which is:

$$U(P) = \iint_S \vec{V}(Q,P) \cdot \vec{n} dS \tag{4-1}$$

Where

$$V(Q,P) = \frac{1}{4\pi?}\left\{ U(Q)\nabla_Q \frac{\exp(iks)}{s} - \frac{\exp(iks)}{s}\nabla_Q U(Q) \right\} \tag{4-2}$$

Where a monochromatic scalar wave field with frequency ω could be written as

$$V(x,y,z,t) = U(x,y,z)\exp(-i\omega t) \tag{4-3}$$

And *U* satisfies the Helmholtz equation

$$\left(\nabla^2 + k^2\right)U = 0 \tag{4-4}$$

n is the unit inward normal to S, and s is the distance from observation point P to point Q on aperture.

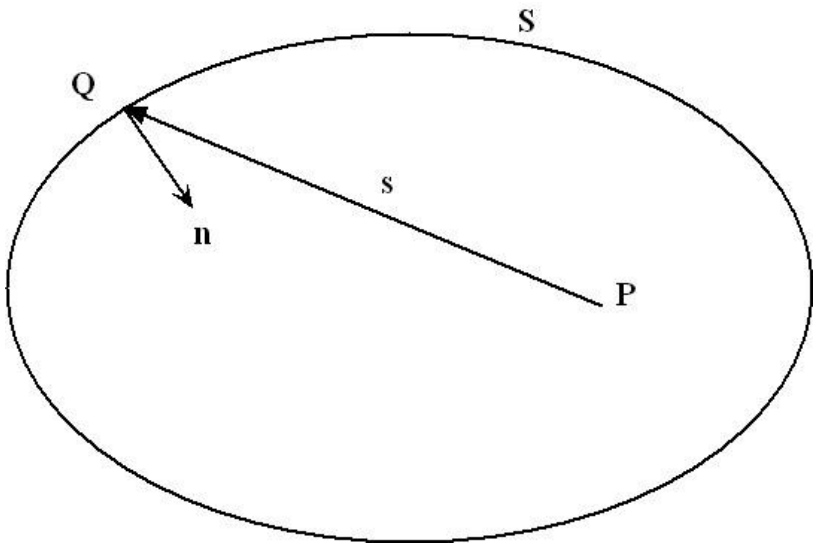

Fig. 4.1. Illustrating the Helmholtz-Kirchhoff integral theorem.

There is a way to express it as a curl of an associated vector potential W(P,Q)

$$\vec{V}(P,Q) = \nabla_Q \times \vec{W}(P,Q) \tag{4-5}$$

Through the use of the Stokes theorem, Kenro Miyamoto and Emil Wolf found this equation could be deduced to

$$U(P) = \sum_j F_j(P) + U_B(P) \tag{4-6}$$

This separation forms the basic equation of the Boundary Diffraction Wave (BDW) theory. U_B represents the boundary diffraction wave coming from the boundary Γ of the diffraction aperture. This expression is given by the contour integral of **W**

$$U_B(P) = \int_\Gamma \vec{W}(P,Q) \cdot d\vec{l} \tag{4-7}$$

The vector potential **W** associated with a given field U(Q) incident upon the aperture may be expressed as

$$\vec{W}(P,Q) = \frac{e^{iks}}{4\pi s}\hat{s} \times \frac{\nabla_Q}{\left(ik + \hat{s}\cdot\nabla_Q\right)}U(Q) \qquad (4\text{-}8)$$

Where $k=2\pi/\lambda$. The distance PQ is denoted by s; $\hat{s}$ is the corresponding unit vector (see Fig. 4.2).

The F_j term represents the integral contribution of singular points Q_j on the closed surface S. In application of the Stokes theorem to Equation (4-1), these singular points Q_j are dealt with by surrounding them with very small circles of radii σ_j. When the radii σ_j close to zero, contour integrals can be derived (performed clockwise, as seen from P) along the perimeters Γ_j

$$F_j(P) = \lim_{\sigma_j \to 0} \int_{\Gamma_j} \vec{W}(P,Q_j)\cdot d\vec{l} \qquad (4\text{-}9)$$

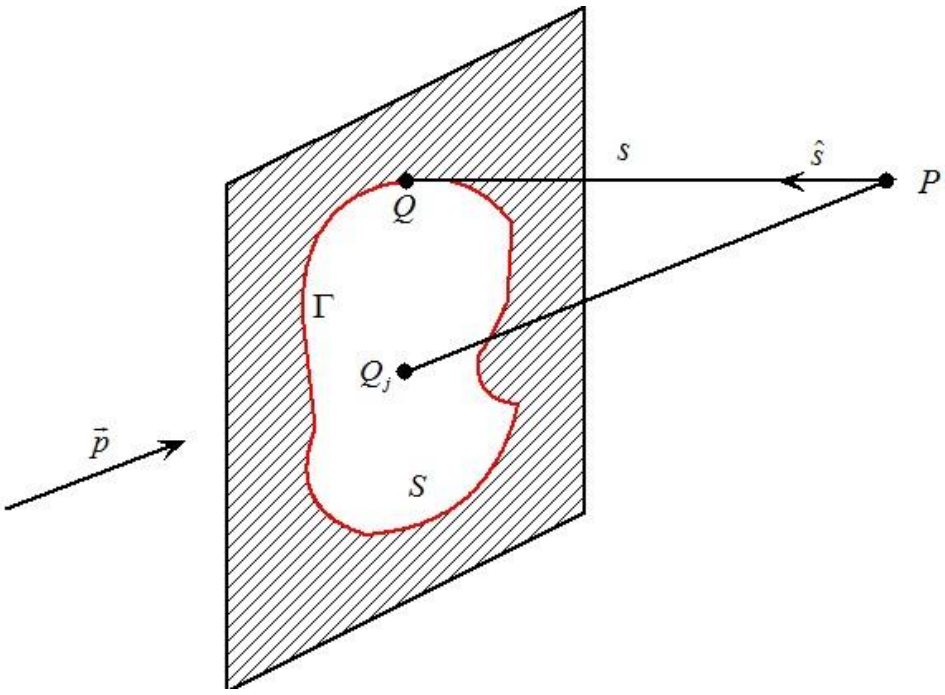

Fig. 4.2. Geometry of the diffraction problem.

According to Equation (4-9), when the incident wave upon the diffracting aperture is either plane or spherical, the term F_j in Equation (4-6) represents precisely the incident wave, propagating freely to the observation point P according to the laws of geometrical optics when there is no any obstacles. In the case where there are no singularities $W(P,Q_j)$ in the aperture, the geometrical wave is zero which physically means the observation point P lies in the optical shadow region.

4.2 Asymptotic representation of BDW for Gaussian beam incident upon a half-screen

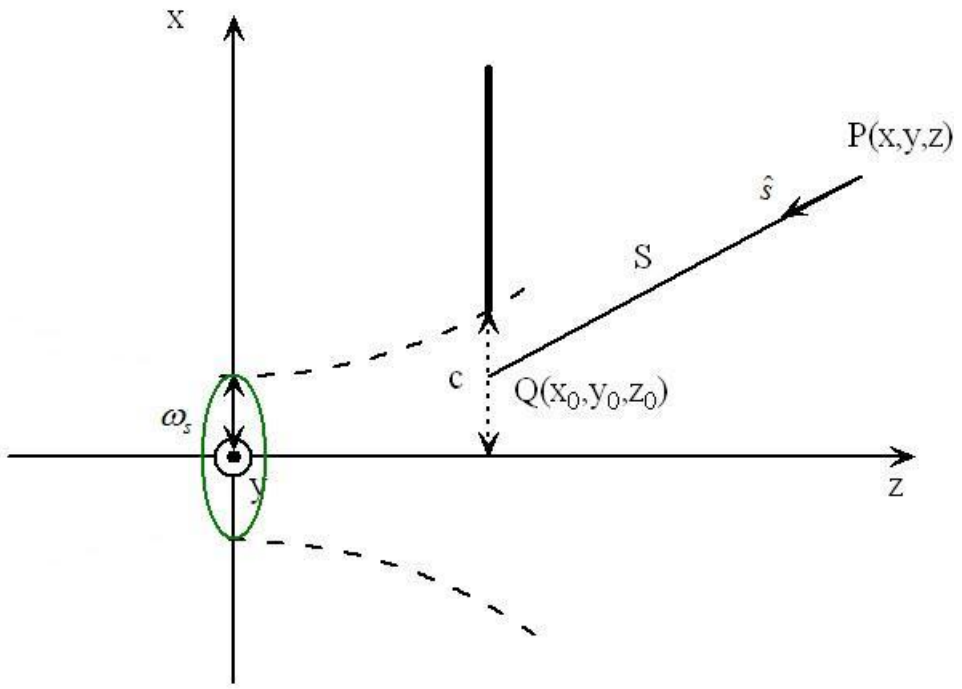

Fig. 4.3. Gaussian Beam diffraction by half screen.

Let a Gaussian beam be normally incident upon a screen in a half-plane x>c, $z=z_0$, as shown in Fig. 4.3. The field of the incident Gaussian beam could be written as [7]:

$$U_i(x,y,z) = \frac{q(0)}{q(z)} \exp\left[ik\phi(x,y,z)\right]$$

$$\text{Where} \quad \phi(x,y,z) = z + (x^2 + y^2)/2q(z) \tag{4-10}$$

$$q(z) = z - \frac{ib}{2}$$

$$b = k\omega_s^2 \qquad (k = 2\pi/\lambda)$$

The incident beam is assumed to propagate along the z direction and to have the smallest spot size ω_s at z=0.

Following the BDW theory, the diffracted field U(P) at an observation point P is

$$U(P) = \sum_j F_j(P) + U_B(P) \tag{4-11}$$

The first term contains the contributions from the singularities of a vector potential W(P,Q) on a plane x<c, z=z_0. Within the paraxial approximation $x_0^2 + y_0^2 \ll |q(z_0)|^2,\ \lambda \ll \omega_s$, according to Equation (4-8) the vector potential **W**(P,Q) for the Gaussian beam is:

$$\overrightarrow{W}(P,Q) = U_i(Q)\frac{e^{iks}}{4\pi s}\frac{\hat{s}\times\nabla_Q\phi}{\left(1+\hat{s}\cdot\nabla_Q\phi\right)} \tag{4-12}$$

$$\nabla_Q\phi = \frac{x_0}{q(z_0)}\hat{x} + \frac{y_0}{q(z_0)}\hat{y} + \left[1 - \frac{x_0^2+y_0^2}{2q(z_0)^2}\right]\hat{z} \tag{4-13}$$

For the paraxial region: $|x_0 - x|^2 + |y_0 - y|^2 \ll |z_0 - z|^2$, we have the approximation

$$s \approx Z + \left[\left(x_0 - x\right)^2 + \left(y_0 - y\right)^2\right]/2Z \quad \text{(for phase term)}$$

$$s \approx Z \quad \text{(for amplitude term)} \tag{4-14}$$

$$\hat{s} \approx \left[\left(x_0 - x\right)\hat{x} + \left(y_0 - y\right)\hat{y} - Z\hat{z}\right]/Z$$

Where Z=(z-z0) is the distance between point P and its projection on the screen, and the vectors $\hat{x}, \hat{y}$ and $\hat{z}$ are the unit vectors in the x, y, and z directions respectively.

The singularities of the vector potential $\vec{W}$ are determined from the denominator of the right-hand side of Equation (4-12):

$$s\left(1+\hat{s}\cdot\nabla_Q\phi\right)=\frac{1}{2Z}\left\{\left[x_0\frac{q(z)}{q(z_0)}-x\right]^2+\left[y_0\frac{q(z)}{q(z_0)}-y\right]^2\right\}=0 \qquad (4\text{-}15)$$

From Equation (4-15), two singular points $P_1(x_0^1, y_0^1, z_0)$ and $P_2(x_0^2, y_0^2, z_0)$ of the vector potential $\vec{W}$ on the plane of the aperture in real space are

$$x_0^1=\frac{x-\gamma y}{\alpha(1+\gamma^2)} \quad y_0^1=\frac{\gamma x+y}{\alpha(1+\gamma^2)}$$
$$x_0^2=\frac{x+\gamma y}{\alpha(1+\gamma^2)} \quad y_0^2=\frac{-\gamma x+y}{\alpha(1+\gamma^2)} \qquad (4\text{-}16)$$

Where $\frac{q(z)}{q(z_0)}=\alpha+\beta i, \quad \gamma=\frac{\beta}{\alpha}$

It can easily be shown that the contribution from each singularity P1 and P2 is equal to a half of the unperturbed incident beam Ui(P) at P. Therefore the first term in Equation (4-11) is represented as

$$\sum_{j=1}^{2}F_j(P)=\left[E\left(x_h^1-x\right)+E\left(x_h^2-x\right)\right]U_i(P)/2 \qquad (4\text{-}17)$$

Where E(τ) is the unit step function and x_h^1 and x_h^2 are the values of x when the singularities P_1, and P_2 , respectively, are on the boundary of the half-screen, i.e.

$$x_h^1 = \alpha c\left(1+\gamma^2\right)+\gamma y$$
$$x_h^2 = \alpha c\left(1+\gamma^2\right)-\gamma y \tag{4-18}$$

The second term $U_B(P)$ in Equation (3.11) is the boundary diffraction wave given by

$$U_B\left(P\right) = \int_{\Gamma} \overrightarrow{W}(P,Q)\cdot \hat{l}dl \tag{4-19}$$

where $\hat{l}$ is the unit vector tangential to the boundary Γ of the half-screen. And the contour integral should be taken counterclockwise when viewed from P. In derivation of Equation (4-16), the contribution only from the small area close to $(c,0,z_0)$ because the field of the incident Gaussian beam vanishes rapidly away from the propagation axis. By substituting Equation (4-13) and (4-14) into Equation (4-12), $U_B(P)$ is represented as

$$U_B\left(P\right) = \int_{-\infty}^{\infty} G(y_0)\exp\left[ikd\left(y_0\right)\right]dy_0 \tag{4-20}$$

Where

$$d\left(y_0\right) = q\left(z_0\right)+\frac{c^2+y_0^2}{2q\left(z_0\right)}+Z+\frac{(c-x)^2+(y_0-y)^2}{2Z}$$
$$G\left(y_0\right) = \frac{q(0)q\left(z_0\right)\left[x-c-cZ/q\left(z_0\right)\right]}{2\pi q^2\left(z\right)\left(y_0-y_p^1\right)\left(y_0-y_p^2\right)}e^{-kb/2} \tag{4-21}$$

Where y_p^1 and y_p^2 are poles of the integrand in Equation (4-20)

$$y_p^1 = \frac{q(z_0)}{q(z)} y - ic\left[1 - \frac{q(z_0)}{cq(z)} x\right]$$
$$y_p^2 = \frac{q(z_0)}{q(z)} y + ic\left[1 - \frac{q(z_0)}{cq(z)} x\right] \qquad (4\text{-}22)$$

It is difficult to obtain analytical result of the boundary-diffraction wave given by Equation (4-20). In high-frequency regions, however, the wave number k is so large that the integral given by Equation (4-20) can be evaluated approximately by the steepest-descent method. The major contributions to $U_B(P)$ come from the poles y_p^1 and y_p^2 and the saddle point

$$y_s = \frac{q(z_0)}{q(z)} y \qquad (4\text{-}23)$$

Let x_s denote the value of x when two poles y_p^1 and y_p^2 are on the steepest-descent path (SDP), i.e., x_s is determined from $\mathrm{Re}[d(y_p^1)] = \mathrm{Re}[d(y_s)]$; then

$$x_s = c\left[\frac{4z^2 + b^2}{4z_0 z + b^2} + \frac{2b(z - z_0)}{4zz_0 + b^2}\left(\frac{4z^2 + b^2}{4z_0^2 + b^2}\right)^{1/2}\right] \qquad (4\text{-}24)$$

We define $x = x_s$, as the shadow boundary.

In the deformation of the path of integration from $-\infty$ to ∞ into the SDP, some poles are encountered. The number of poles encountered depends on the location of observation point P. In the case in which $x_h^2 < x_s < x_h^1$, it is found that no pole is encountered for region $x < x_h^2$, pole y_p^2 for $x_h^2 < x < x_s$, pole y_p^1 for x_s

$<x< x_h^1$, and no pole for $x_h^1<x$. Therefore the boundary diffraction wave is represented as

$$U_B(P)=\left[E\left(x-x_h^1\right)+E\left(x-x_h^2\right)-2E\left(x-x_s\right)\right]2\pi i\kappa e^{ikd\left(y_p^1\right)} + \int_{SDP} G(y_0)\mathrm{e}^{ikd(y_0)}\,dy_0 \tag{4-25}$$

Where κ is the residue of $G(y_0)$ at pole y_p^1,

$$\kappa=-\frac{iq(0)}{4\pi q(z)}e^{-kb/2} \tag{4-26}$$

Using Appendix D we will get

$$\int_{SDP} G(y_0)\mathrm{e}^{ikd(y_0)}\,dy_0 \approx \mp 2\pi i\kappa\,\mathrm{e}^{ikd\left(y_p^1\right)}\,erfc\left(\pm i\left\{ik\left[d(y_s)-d\left(y_p^1\right)\right]\right\}^{1/2}\right) + \sqrt{\pi/k}\,\mathrm{e}^{ikd(y_s)}\left(G(y_s)\left[\frac{i2q(z_0)Z}{q(z)}\right]^{1/2}+\frac{2\kappa}{\left\{i\left[d(y_s)-d\left(y_p^1\right)\right]\right\}^{1/2}}\right) \tag{4-27}$$

$$\left(x \lesseqgtr x_s\right)$$

Where erfc(τ) is the complementary error function defined by

$$erfc(\tau)=\frac{2}{\sqrt{\pi}}\int_{\tau}^{\infty}e^{-x^2}dx \tag{4-28}$$

After some calculation of the right-hand side of Equation (4-27), it is found that the two parts in second term cancel each other, so that only the first term remains.

Use of Equations (4-17), (4-26), and (4-27) in Equation (4-11) yields the uniform asymptotic representation of the diffracted field $U_K(P)$ as follows:

$$U_k(P)\approx U_G(P)+U_D(P) \tag{4-29}$$

Where $U_G(P)$ and $U_D(P)$ are the geometrical-optics and diffraction components, respectively. These are given by

$$U_G(P) = E(x_s - x)U_i(P)$$
$$U_D(P) = D_u\left[\frac{q(z_0)}{q(z)Z}\right]^{1/2} \exp\left[iks(Q_d)\right]U_i(Q_d) \quad (4\text{-}30)$$

Where $s(Q_d)$ is the complex distance from saddle point Q_d (c,y_s,z_0) to observation point P,

$$s(Q_d) = Z + \frac{(x-c)^2 + (y-y_s)^2}{2Z} \quad (4\text{-}31)$$

the first factor D_u in Equation (4-30) is given by

$$D_u = \mp\frac{1}{2}erfc\left(\pm i\left\{ik\left[d(y_s) - d\left(y_p^1\right)\right]\right\}^{1/2} \times \left[\frac{q(z_0)Z}{q(z)}\right]^{1/2} e^{ik\left[d\left(y_p^1\right) - d(y_s)\right]}\right) \quad (4\text{-}32)$$
$$(x \lesseqgtr x_s)$$

4.3 Diffraction Field in the Backward-scattering Region

Since we will compute reflection by reflector antennas, we are only interested in the diffracted field in the backward-scattering region (z<0). We try to find an equivalent model to describe the diffracted field in the backward-scattering region. As we discussed in reflection part, reflected wave in the backward scattering region is equivalent to an image beam at the opposite side of the half-screen, the same in magnitude but opposite in sign to the incident beam. The image beam is propagating in the -z direction and diffraction has to be

described in a new coordinate system with the transformed xr, yr and zr axes pointing in the -x, y and -z directions, respectively. And in the equivalent model the equivalent half screen must be complementary to the real half screen to generate a shadow region in the lower half-space (x<0). The boundary location should be the same since diffraction wave depends on the location of the edge and not on the orientation of the half-screen. Fig. 4.4 shows the equivalent geometry for calculating the diffracted field in the backward-scattering region. Fig. 4.5 shows the backward-scattering field for different Gaussian beam spot size. Fig. 4.6 shows the backward-scattering field for different parameter c.

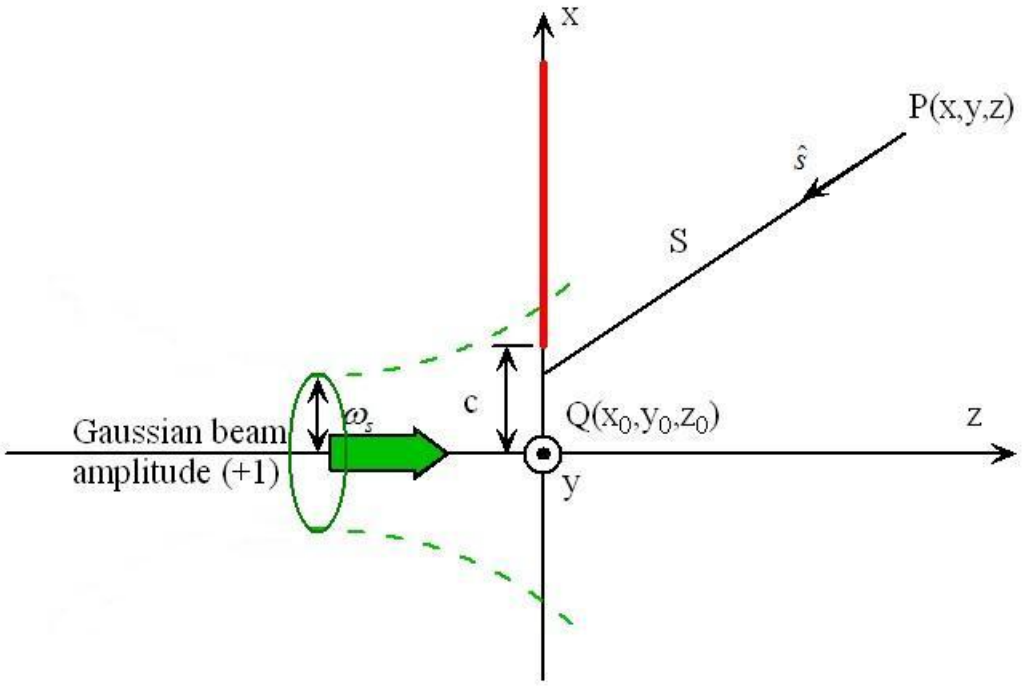

(a)

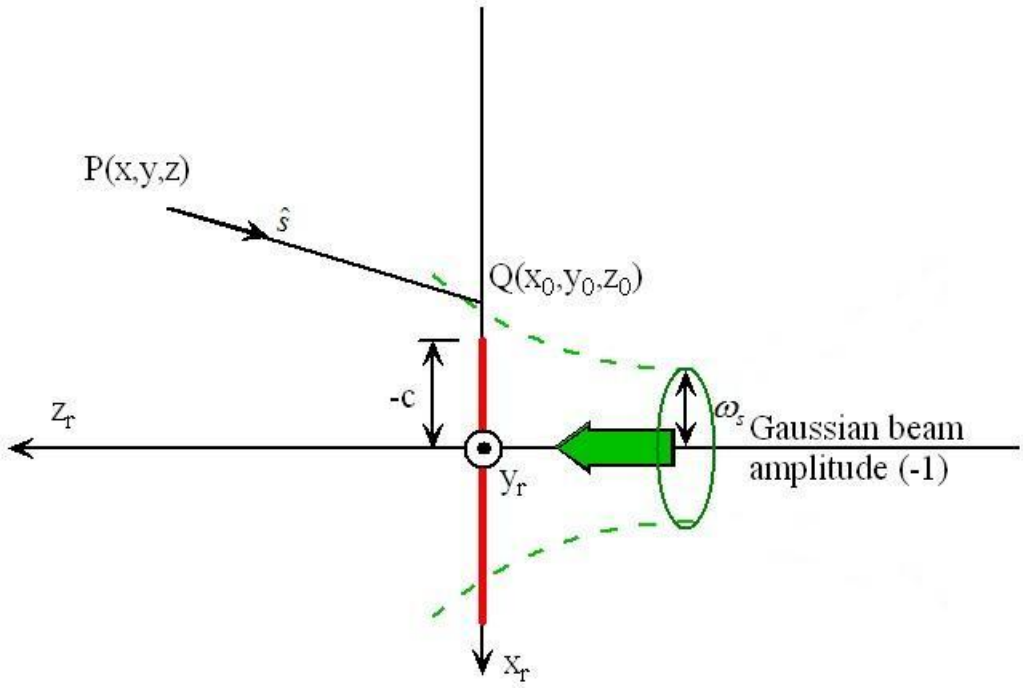
P(x,y,z)
$\hat{s}$
Q(x_0,y_0,z_0)
-c
z_r
ω_s
Gaussian beam
amplitude (-1)
y_r
x_r

(b)

Fig. 4.4. Origin and equivalent geometry for determining the diffracted field in the backward-scattering region.

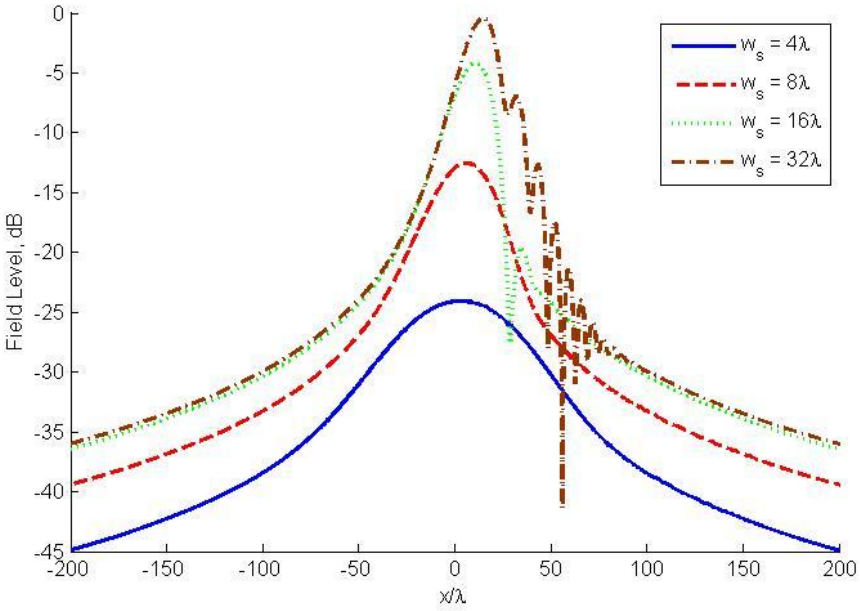

Fig. 4.5. Backscattered field for various beam spot sizes c=0, z=-400λ, z_0=0.

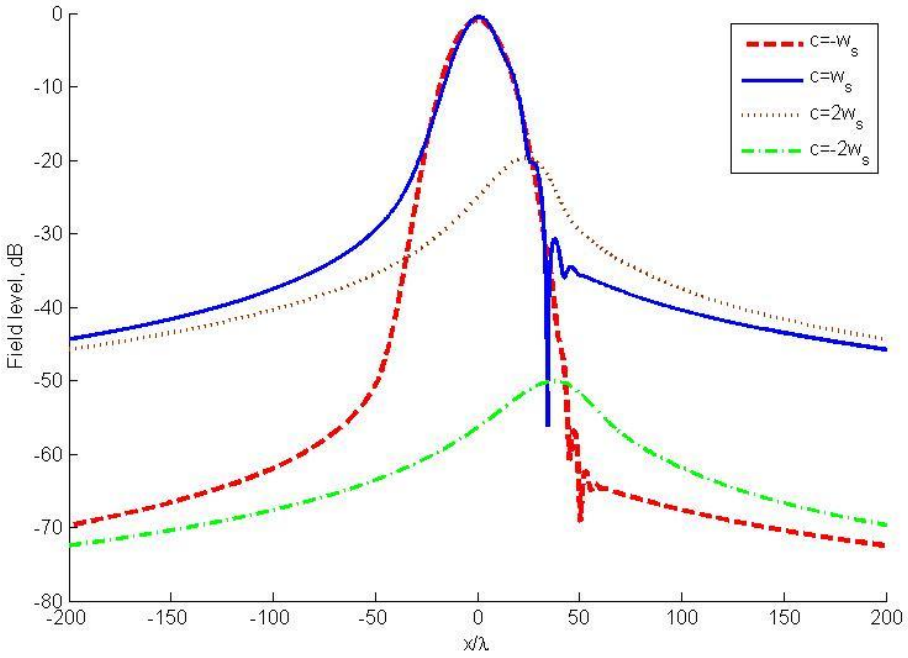

Fig. 4.6. Backscattered field for various c, $w_s=16\lambda$, $z=-400\lambda$, $z_0=0$.

However when each Gaussian beam hit the reflector edge, the propagation direction of Gaussian beam may be not perpendicular to the reflector. Fig. 4.7 depicts the geometry of the discussed problem, showing three different coordinate systems: the transmitted beam-related co-ordinate system (x_t, y_t, z_t), the reflected beam related co-ordinate system (x_r, y_r, z_r) and the half-screen based co-ordinate system (x, y, z). The intersection point between the incident and reflected beam axes is the origin point of the half-screen based coordinate system. Since normal incidence is assumed with respect to the polar angle, the y-direction is the same for all three co-ordinate systems. Let φ_0 be the incidence angle of negative propagation direction ($-\hat{z}_t$) and half-screen tangential direction ($\hat{z}$). The

observation point is described in the half-screen based cylindrical (ρ, φ, y) coordinate system. The transmitted and reflected beams propagate in the ($\pi+\varphi_0$) and ($\pi-\varphi_0$) direction, respectively. Their co-ordinate systems are expressed regarding to the half-screen co-ordinate system by simple translation as

$$\begin{pmatrix} z_t \\ x_t \end{pmatrix} = \rho \begin{pmatrix} \cos\left(\phi - \left(\pi + \phi_0\right)\right) \\ \sin\left(\phi - \left(\pi + \phi_0\right)\right) \end{pmatrix} + \begin{pmatrix} z_e \cos\left(\phi\right) \\ 0 \end{pmatrix}$$
$$\begin{pmatrix} z_r \\ x_r \end{pmatrix} = \rho \begin{pmatrix} \cos\left(\phi - \left(\pi - \phi_0\right)\right) \\ \sin\left(\phi - \left(\pi - \phi_0\right)\right) \end{pmatrix} + \begin{pmatrix} z_e \cos\left(\phi_0\right) \\ 0 \end{pmatrix} \quad (4\text{-}33)$$

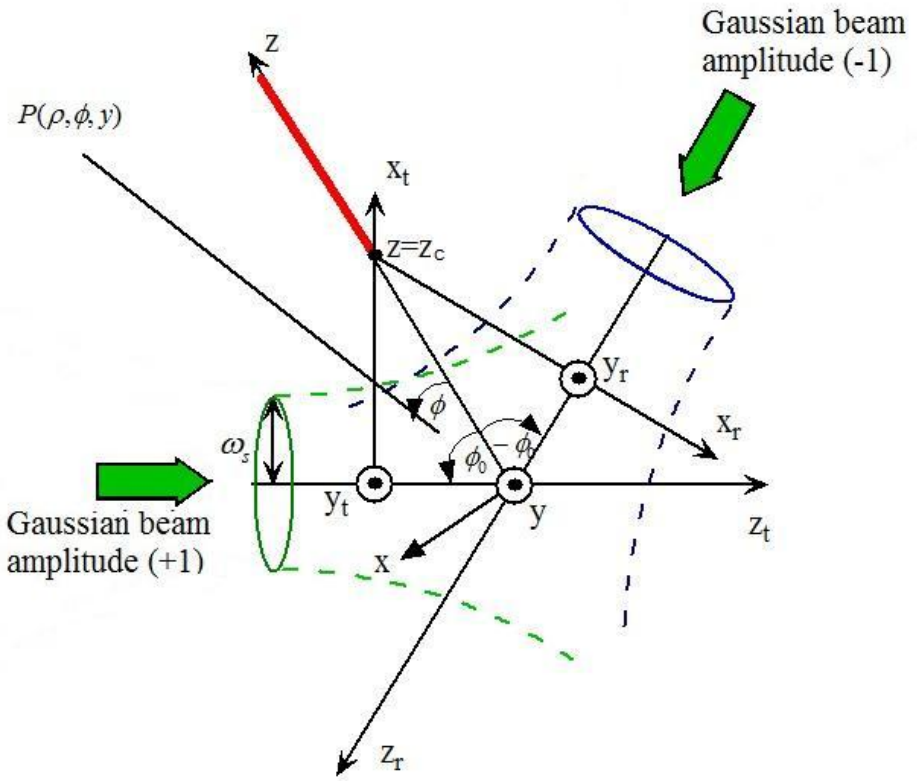

Fig. 4.7. Equivalent geometry for determining the diffracted field in the backward-scattering region at oblique incident.

Since the boundary diffraction wave is obtained as a line integral along the edge and does not depend on the orientation of the half-screen, we can apply it regarding to the reflected beam co-ordinate system (x_r, y_r, z_r). The offset distance c from the edge (see Fig. 4.4(a)) is related to the axial position z. In the half-screen based co-ordinate system (Fig. 4.7), it is $c=z_e\sin(\varphi_0)$.

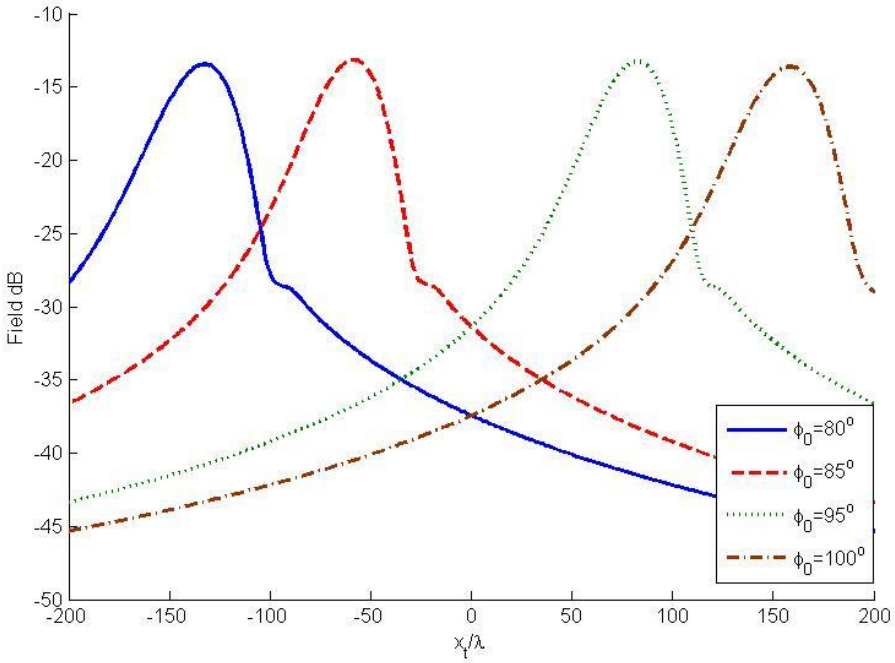

Fig. 4.8. Backscattered field for various orientations of the half-screen $w_s=8\lambda$, $c=0$, $z_t=-300\lambda$, $z_0=100\lambda$.

With respect to the polarization, we use normal incidence ($\theta= 90^o$). The field has been calculated with the half-beamwidth w_s to be eight wavelengths. The parameter *c* equals zero.

It would be great if we can derive a solution for non-normal incidence with respect to the polar angle as we did in reflection part. Unfortunately, in our general problem the incident Gaussian beam cannot be separated into three Cartesian coordinates as people do in classical GTD problem. However we can only consider the normal incidence part as a good approximation. Since in quasi-optical systems the distance between the reflectors is usually much larger than their diameter such that the beams are well located in the validity of the paraxial approximation and the incident condition is close to normal incidence. The error is small enough to be neglected. So the conclusion is that for incidence angles close to 90^{o} the results for the equivalent geometry in Fig. 4.7 can still be valid.

CHAPTER 5

PARALLEL COMPUTATION RESULT

The field on a plane $z \geqslant 0$ is the superposition of all Gaussian beams. Since these Gaussian beams are independent, they can be calculated on different processors. Fig. 5.1 illustrates the parallel scheme for computation task assignment. First, all A_{mnuv} will be calculated on the master processor. Then all information about these Gaussian beams, stored in [A0], will be distributed to all slave processors. According to number of processor N, [A0] is equally divided into N segments, of which each will pass to the relevant processor. Every processor will produce the field [Un] for the output plane from their assigned Gaussian beams and then pass the output field to the master processor which will add up output field.

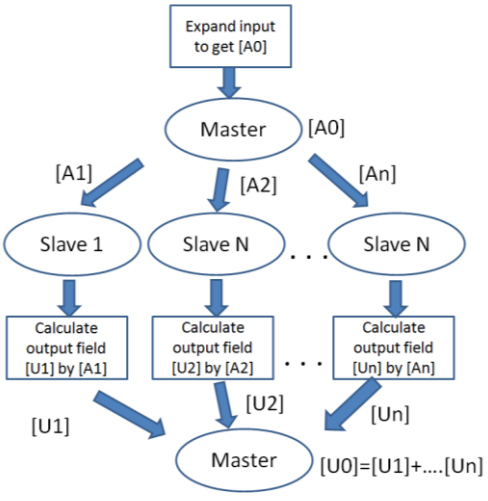

Fig. 5.1. Program flow chat for parallel computation.

The reflector antenna system in Fig. 5.2 is analyzed to demonstrate the efficiency and effectiveness of this algorithm. The source is a Huygens source and the radiated electrical field could be written as [12]

$$E_y = N\frac{e^{jkr}}{r}e^{kb\cos\theta}(1+\cos\theta) \tag{5-1}$$

If the taper is specified to A dB (A < 0) at the angle θ0, b can be obtained as

$$b = \frac{20\log\left(\frac{(1+\cos\theta_0)}{2}\right) - A}{20k(1-\cos\theta_0)\log(e)} \tag{5-2}$$

In this example we choose A=-6dB. At 30GHz the reflector has a diameter of 40λ. The source is located at one focal point of the hyperboloid reflector, and the image of the source is the other focal point of the hyperboloid reflector. The input plane is chosen 0.8m away from the feed. The elementary beams in Gaussian beam expansion are 12 wavelengths wide i.e., L=6λ. The input plane is 52λ by 52λ with sampling shift λ. The output plane is 2m away from the reflector. Results, well agreed with the previous paper [1], are shown in Fig. 5.2 (b). In Fig. 5.2 (c), we list the computation time on Arizona State University Saguaro cluster. The developed parallel algorithm is based on Message Passing Interface (MPI) [28]. For this simulation, efficiency has greatly increased when 16 processors are used.

When using 24 processors, communications between computers degrades the performance.

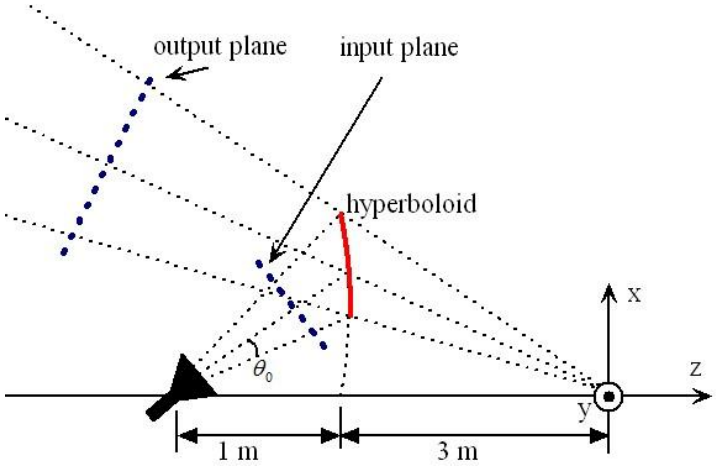

(a)

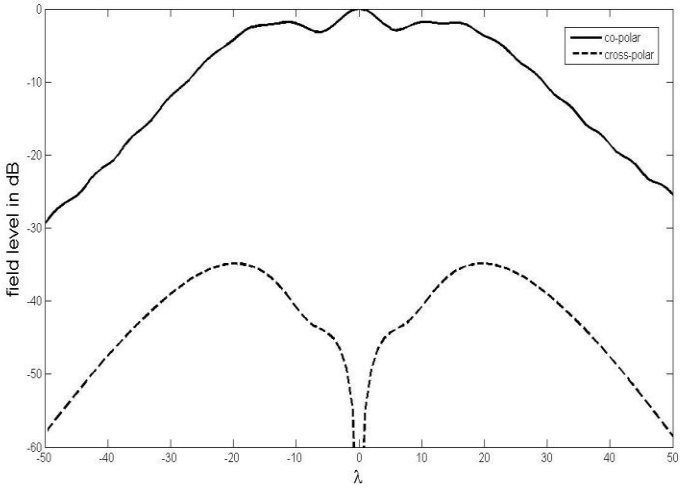

(b)

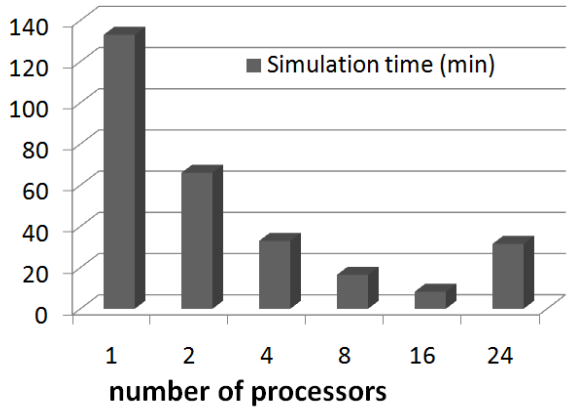

(c)

Fig. 5.2. Reflector antenna simulation.

(a) geometry of antenna; (b) near field from reflector antenna at output plane; (c) simulation time comparison for parallel computation.

CHAPTER 6

COIFMAN WAVELETS AND INTERVALLIC COIFLETS

6.1 Multi-resolution Analysis

The study of orthogonal wavelets begins with the multi-resolution analysis (MRA) which is defined as a nested sequence of closed subspace $\{V_j\}_{j\in Z}$ of $L^2(R)$, with the following properties:

1. $\cdots \subset V_{-1} \subset V_0 \subset \cdots \subset L^2(R)$
2. $v(x) \in V_j \Leftrightarrow v(2x) \in V_{j+1}$
3. $v(x) \in V_0 \Leftrightarrow v(x+1) \in V_0$
4. $\bigcap_j V_j = \{0\}, closure\left(\bigcup_j V_j\right) = L^2(R)$
5. $\exists \varphi(t) \in V_0$ such that $\{\varphi(t-n)\}$ form a Riesz basis of V_0

Correspondingly physical meaning of these five properties is:

- The nested sub-spaces implies that information in coarser V_j space is contained in the finer spaces
- V_j is dilation invariant subspace. This property allows us to multigrid basis functions according to the nature of the solution. In the rapidly varying regions the resolution could be very fine, while in the opposite situation the basis could be very coarse.
- Translation invariant V_j.
- Errors and residues in wavelet expansion.
- Riesz basis condition will be used to drive and prove convergence.

If we have basis $\varphi(t) \in V_0$, then $\sqrt{2}\varphi(2t-k) \in V_1$, according the MRA properties we should have

$$\varphi(t) = \sum_k h_k \sqrt{2}\varphi(2t-k), \qquad \{h_k\} \in l^2, t \in R \tag{6-1}$$

Equation (6-1) is called the dilation equation, and is one of the most important equations in the field of wavelets. The MRA allow us to expand a function $f(t)$ in terms of basis functions, consisting of the scalets and wavelets. Any function $f \in L^2(R)$ can be projected onto V_m by means of a projection operator P_{Vm}, defined as $P_{Vm}f = f^m \coloneqq \sum_n f_{m,n}\varphi_{m,n}$, where $f_{m,n}$ is the coefficient of expansion of f on the basis $\varphi_{m,n}$. From the previously listed MRA properties, it can be proved that $\lim_{m\to\infty}\|f - f^m\| = 0$, which means a function can be approximated with any precision by increasing the resolution in MRA.

6.2 Coifman Wavelets (Coiflets)

An orthonormal wavelet system with compact support is called the Coifman wavelet system of order L if $\varphi(t)$ have $L-1$ vanishing moments, which is

$$\int t^l \varphi(t)dt = 0, \quad l = 1, 2, \ldots, L-1 \tag{6-2}$$

And

$$\int \varphi(t)dt = 1 \tag{6-3}$$

The nonzero support of the Coiflets of order $L = 2K$ is $[-L, 2L-1]$.

Property of (6-2) will yield:

$$\sum k h_k = 0. \tag{6-4}$$

In order to let Coiflets to be orthonormal basis, following equations can be derived

$$\begin{aligned} &\sum_k h_k = \sqrt{2} \\ &\sum_k (-1)^k h_k = 0 \\ &\sum_k h_k h_{k-2n} = \delta_{0n} \end{aligned} \tag{6-5}$$

According to (6-4) and (6-5), for $L=4$, h_k result is list in Table 1

Table 1 h_k coefficient for $L=4$ Coiflets dilation equation

n	$\boldsymbol{h_k/\sqrt{2}}$
-4	1.15876e-2
-3	-2.932014e-2
-2	-4.76396e-2
-1	2.73021047e-1
0	5.7468239e-1
1	2.948671937e-1
2	-5.408561e-2
3	-4.20264805e-2
4	1.67444101e-2
5	3.96788361e-3

6	-1.2892033e-3
7	-5.095054e-4

6.3 Construction Coiflets by Recursion & Iteration

6.3.1 Average Current Sensing Recursion method

For $L=4$ Coiflets, it has support [-4, 7]. At boundary, $\varphi(-4)=0,\ \varphi(7)=0,$ other wise Coiflets won't be continuous. Plug in other integer points in support to dilation equation (6-1)

$$
\begin{aligned}
\varphi(-3) &= h_{-4}\sqrt{2}\varphi(-2) + h_{-3}\sqrt{2}\varphi(-3)\\
\varphi(-2) &= h_{-4}\sqrt{2}\varphi(0) + h_{-3}\sqrt{2}\varphi(-1) + h_{-2}\sqrt{2}\varphi(-2) + h_{-1}\sqrt{2}\varphi(-3)\\
\varphi(-1) &= h_{-4}\sqrt{2}\varphi(2) + h_{-3}\sqrt{2}\varphi(1) + h_{-2}\sqrt{2}\varphi(0) + h_{-1}\sqrt{2}\varphi(-1)\\
&\quad + h_{0}\sqrt{2}\varphi(-2) + h_{1}\sqrt{2}\varphi(-3)\\
\varphi(0) &= h_{-4}\sqrt{2}\varphi(4) + h_{-3}\sqrt{2}\varphi(3) + h_{-2}\sqrt{2}\varphi(2) + h_{-1}\sqrt{2}\varphi(1)\\
&\quad + h_{0}\sqrt{2}\varphi(0) + h_{1}\sqrt{2}\varphi(-1) + h_{2}\sqrt{2}\varphi(-2) + h_{3}\sqrt{2}\varphi(-3)\\
\varphi(1) &= h_{-4}\sqrt{2}\varphi(6) + h_{-3}\sqrt{2}\varphi(5) + h_{-2}\sqrt{2}\varphi(4) + h_{-1}\sqrt{2}\varphi(3)\\
&\quad + h_{0}\sqrt{2}\varphi(2) + h_{1}\sqrt{2}\varphi(1) + h_{2}\sqrt{2}\varphi(0) + h_{3}\sqrt{2}\varphi(-1)\\
&\quad + h_{4}\sqrt{2}\varphi(-2) + h_{5}\sqrt{2}\varphi(-3)\\
\varphi(2) &= h_{-2}\sqrt{2}\varphi(6) + h_{-1}\sqrt{2}\varphi(5) + h_{0}\sqrt{2}\varphi(4) + h_{1}\sqrt{2}\varphi(3)\\
&\quad + h_{2}\sqrt{2}\varphi(2) + h_{3}\sqrt{2}\varphi(1) + h_{4}\sqrt{2}\varphi(0) + h_{5}\sqrt{2}\varphi(-1)\\
&\quad + h_{6}\sqrt{2}\varphi(-2) + h_{7}\sqrt{2}\varphi(-3)\\
\varphi(3) &= h_{0}\sqrt{2}\varphi(6) + h_{1}\sqrt{2}\varphi(5) + h_{2}\sqrt{2}\varphi(4) + h_{3}\sqrt{2}\varphi(3) +\\
&\quad h_{4}\sqrt{2}\varphi(2) + h_{5}\sqrt{2}\varphi(1) + h_{6}\sqrt{2}\varphi(0) + h_{7}\sqrt{2}\varphi(-1)\\
\varphi(4) &= h_{2}\sqrt{2}\varphi(6) + h_{3}\sqrt{2}\varphi(5) + h_{4}\sqrt{2}\varphi(4) + h_{5}\sqrt{2}\varphi(3)\\
&\quad + h_{6}\sqrt{2}\varphi(2) + h_{7}\sqrt{2}\varphi(1)\\
\varphi(5) &= h_{4}\sqrt{2}\varphi(6) + h_{5}\sqrt{2}\varphi(5) + h_{6}\sqrt{2}\varphi(4) + h_{7}\sqrt{2}\varphi(3)\\
\varphi(6) &= h_{6}\sqrt{2}\varphi(6) + h_{7}\sqrt{2}\varphi(5)
\end{aligned}
\tag{6-6}
$$

Equation (6-6) is typical eigen-value equation. When considering the normalization condition:

$$\sum_{n} \varphi(t-n) = 1 \tag{6-7}$$

We can get values at integer points.

$$\begin{aligned}
&\varphi(-4) = 0 \\
&\varphi(-3) = 0.000750387321579783 \\
&\varphi(-2) = 0.0342775992864935 \\
&\varphi(-1) = -0.147015530207457 \\
&\varphi(0) = 1.23031367372496 \\
&\varphi(1) = -0.162912388827161 \\
&\varphi(2) = 0.0470857907521607 \\
&\varphi(3) = -0.00252723822119367 \\
&\varphi(4) = 2.51783852394600e-05 \\
&\varphi(5) = 2.53035721025110e-06 \\
&\varphi(6) = -2.57183018768425e-09 \\
&\varphi(7) = 0
\end{aligned} \tag{6-8}$$

6.3.2 Iteration method

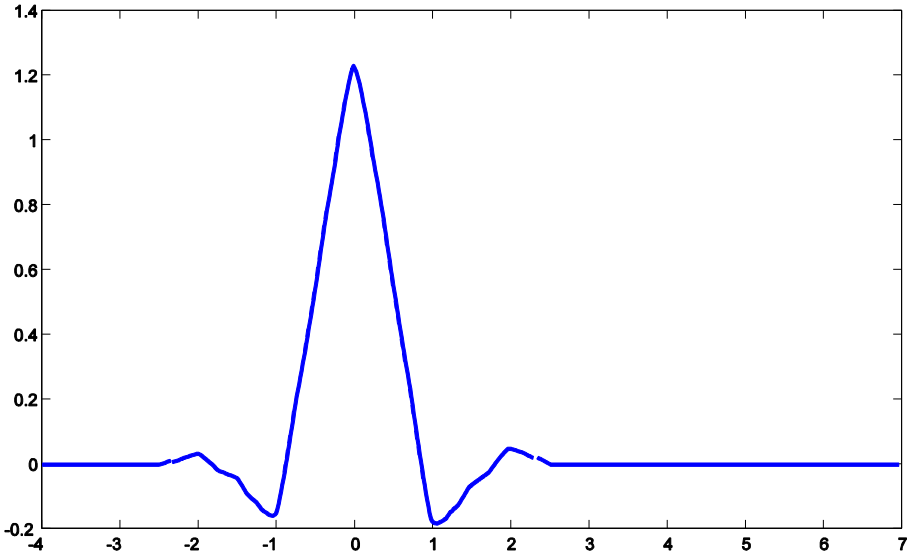

Fig. 6.1. Coiflet for j0=0, k=0, L=4.

After get values at integer points, we may plug half integer points in to dilation equation (6-1)

$$\begin{aligned} &\varphi(-3.5) = h_{-4}\sqrt{2}\varphi(-3) \\ &\varphi(-2.5) = h_{-4}\sqrt{2}\varphi(-1) + h_{-3}\sqrt{2}\varphi(-2) + h_{-2}\sqrt{2}\varphi(-3) \\ &\cdots \end{aligned} \tag{6-9}$$

Utilizing these half-integer points, we may obtain the values at the quarter-integer points. Repeating this process, we shall find the values at any dyadic fraction points. In other words, for Coiflets there is no analytical expression but digital solution. Once we get this 0 level Coiflets $\varphi_{0,0}$ at original point, the other basis should be

$$\varphi_{j_0,k}(t) = 2^{j_0/2}\varphi_{0,0}(2^{j_0}t - k) \tag{6-10}$$

Where j0 represents the level of subspace, k is the shift for each basis. All basis for one subspace is complete orthonormal, which leads

$$\int \varphi_{j_0,m}(t)\varphi_{j_0,n}(t)dt = \delta_{m,n} = \begin{cases} 0 & m \neq n \\ 1 & m = n \end{cases} \tag{6-11}$$

6.4 Coiflets Property

Because of properties (6-2) and (6-3), Coiflets can exhibit *Dirac-δ* sampling property for smooth functions, which is

$$\begin{aligned} &\int_p^q f(x)\varphi(x - x_0)dx = \\ &\int_p^q \left(f(x_0) + f'(x_0)(x - x_0) + \cdots + \frac{f^{L-1}(x_0)(x - x_0)^{L-1}}{(L-1)!} + \cdots \right)\varphi(x - x_0)dx \\ &= f(x_0) + O((x - x_0)^L) \end{aligned} \tag{6-12}$$

Where integration interval [p,q] is the support of $\varphi(x)$.

Dirac-δ function is the extreme example of localization in the spatial domain with infinite number of vanishing moments.

$$\int f(x)\delta(x - x_0)dx = f(x_0) \tag{6-13}$$

The *Dirac-δ* function like nature of the Coiflets allows us to simplify quadrature computation into a single point value, and thus speeds up the matrix element evaluations. As an example of the zero moment property, we present in Table 2 first seven moment integrals for L=4 Coiflet. Comparing to pulse basis for which

one point quadrature rule is $O((x-x_0))$, Coiflet has three exact zero moments and even the fourth moment integral is close to zero.

Table 2 Moment Integrals for L=4 Coiflet

n	Moment integral value
0	1.0000000
1	0.0000000
2	0.0000000
3	0.0000000
4	4.9333e-11
5	-0.1348373
6	3.5308e-10

Table 3 Numerical result for Coiflets properties

Ideal Property	Numerical value from computation
$\int \varphi_{0,0}(t)\varphi_{0,0}(t)dt = 1$	1.000000003387167
$\int \varphi_{0,0}(t)\varphi_{0,1}(t)dt = 0$	0.000000039638602
$\int \varphi_{0,0}(t)dt = 1$	0.99998758604572
$\int t\varphi_{0,0}(t)dt = 0$	-0.000049873707868
$\int t^2\varphi_{0,0}(t)dt = 0$	-0.000199813419603
$\int t^3\varphi_{0,0}(t)dt = 0$	-0.00079826902927

$\int t^4 \varphi_{0,0}(t)dt = 0$	-0.003180400355591

6.5 Intervallic Coiflets on [0, 1]

For any given function which is defined on [0, 1], the function itself may have nonzero value at the two end points, 0 and 1. This condition has limited the application of the Coiflets in periodic problem, since Coiflet is zero at its boundary. An alternate approach, which is less restrictive, is the use of intervallic wavelets. This approach converts a regular wavelet into its corresponding intervallic wavelet within the domain [0, 1].

For L=4, j_0=0 level Coiflets, the nonzero support is 11, namely

$$\text{supp}\{\varphi(x)\} = [-4, 7] \tag{6-14}$$

Then when for any j_0, and k

$$\text{supp}\{\varphi(2^{j_0}x - k)\} = [2^{-j_0}(-4 + k), 2^{-j_0}(7 + k)] \tag{6-15}$$

We divide the regular Coiflets into three groups:

1) The left group, $S_{j_0}^L$, which intercepting the left boundary point 0.
2) The right group, $S_{j_0}^R$, which intercepting the right boundary point 1.
3) Completely situated within [0, 1]. No treatment is necessary.

The two groups, $S_{j_0}^L$ and $S_{j_0}^R$ are treated in a similar manner.

For left group, point 0 should inside of its support, namely

$$\begin{cases} 2^{-j_0}(-4+k) < 0 \\ 2^{-j_0}(7+k) > 0 \end{cases} \tag{6-16}$$

It follows that

$$-7 < k < 4 \tag{6-17}$$

For right group, point 1 should inside of its support, namely

$$\begin{cases} 2^{-j_0}(-4+k) < 1 \\ 2^{-j_0}(7+k) > 1 \end{cases} \tag{6-18}$$

It follows that

$$2^{j_0} - 7 < k < 2^{j_0} + 4 \tag{6-19}$$

We wish to build the left basis functions from the Coiflets in the left group. Ideally these wavelets are orthogonal to the Coiflets in the central group, and orthogonal to the right group basis. Finally they are orthonormal among themselves within the group. Then construction begins with the expansion of the monomials. One approach to make the edge bases is to employ monomials: $x^0, x^1, x^2, \ldots, x^{r-1}$. For any monomial x^r we have:

$$x^r = \sum_k \left\langle x^r, \varphi_{j_0,k} \right\rangle \varphi_{j_0,k}(x) \qquad 0 \le r \le L-1 \tag{6-20}$$

Where $\varphi_{j0,k}$ is unrestricted, namely

$$x \in R$$

And k should be the value indicated (6-17) and (6-19) respectively for left and right edge bases. Next, if $x \in [0,1]$

$$x^r|_{[0,1]} = \sum_k \left\langle x^r, \varphi_{j_0,k} \right\rangle \varphi_{j_0,k}(x)|_{[0,1]} \tag{6-21}$$

So the new left basis functions, $x_{j0,L}^{r}$ (r=0,1,…, L-1) are defined as

$$x_{j0,L}^{r} = \sum_{k \in S^{L}} \left\langle x^{r}, \varphi_{j_0,k} \right\rangle \varphi_{j_0,k}(x)\,|_{[0,1]} \qquad (6\text{-}22)$$

These basis functions are linearly independent but not orthonormal. So we may use Schmidt Cramer orthogonalization method in Appendix. When j0=4, the orthonormalized left and right bases are illustrated in Fig. 6.2 and Fig. 6.3

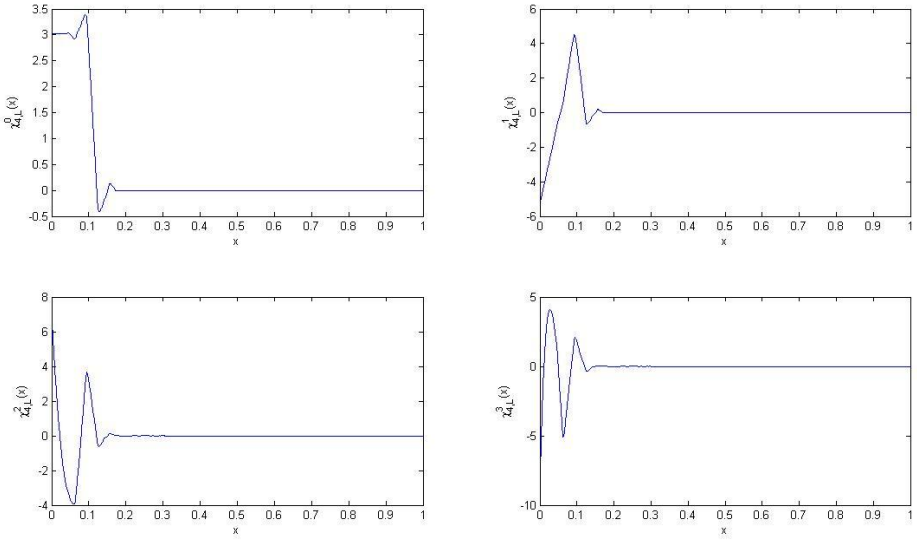

Fig. 6.2. Left-edge basis after orthonormalization.

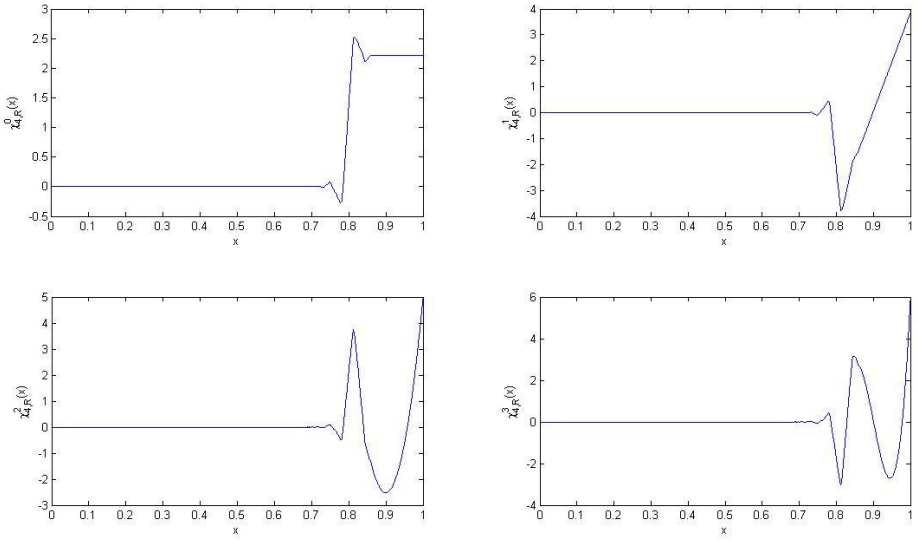

Fig. 6.3. Right-edge basis after orthonormalization.

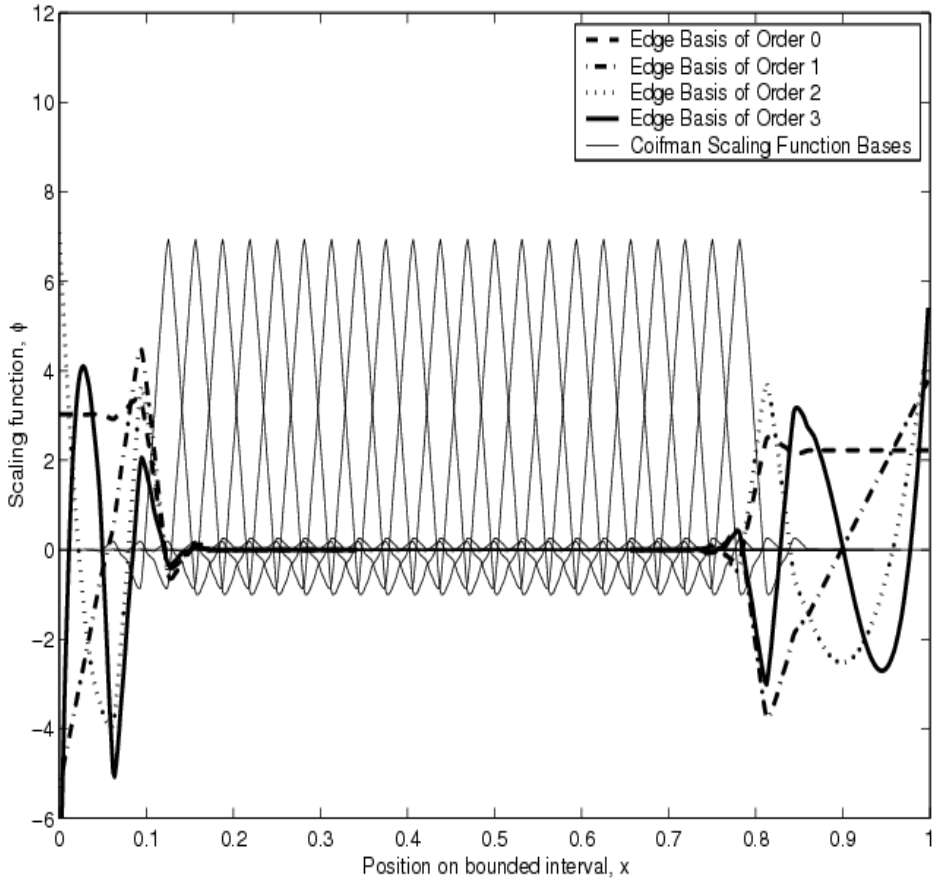

Fig. 6.4. Coifman intervallic scalets when j0=4.

For example, expand the following function

$$y(x)=\begin{cases}2-e^{-x^2/2} \ for & -1\le x<0\\ -x+1 \ for & 0\le x\le 1\end{cases} \tag{6-23}$$

First, we have to rescale the x range, let

$$x'=\frac{x+1}{2} \tag{6-24}$$

Then, $x'\in[0,1]$

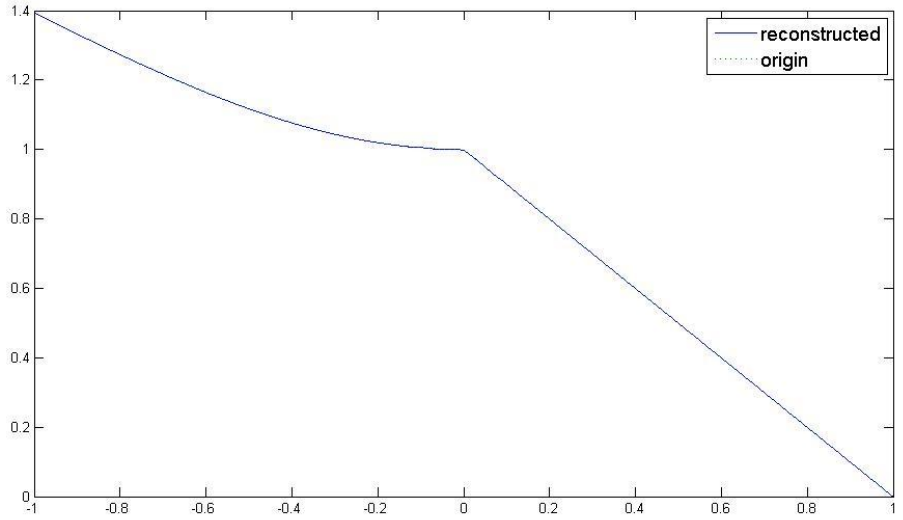

Fig. 6.5. Original function (6-23) and its reconstructed value at level 4 intervallic Coiflets.

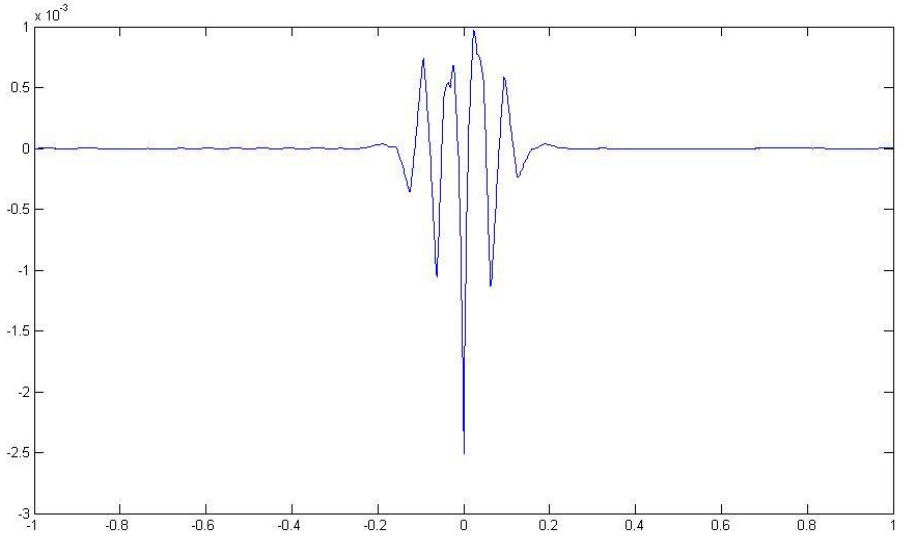

Fig. 6.6. Difference between original function (6-23) and its reconstructed value at level 4 intervallic.

From Fig. 6.6, we can find the main difference between original and reconstructed value is around 0 point. This is because the original function is not smooth at 0 point.

CHAPTER 7 COIFLETS IMPLEMENTATION OF THE MFIE

7.1 Magnetic Integral Equation Formulation (MFIE)

7.1.1 MFIE in spatial domain

For 3-D plane wave scattering by PEC surface, the MFIE [24] is

$$\vec{J}^s(\vec{R}) = 2\vec{n}\times\vec{H}^i(\vec{R}) + \frac{\vec{n}\times}{2\pi}\iint_{S_t}\vec{J}^s(\vec{R}')\times\nabla' g(\vec{R},\vec{R}')ds' \tag{7-1}$$

Where S_t is infinite scattering area and g is 3-D Green's function

$$g(\vec{R},\vec{R}') = \frac{e^{-jk_0\left|\vec{R}-\vec{R}'\right|}}{\left|\vec{R}-\vec{R}'\right|} \tag{7-2}$$

When we consider the doubly periodic cone, (7-1) convert to

$$\begin{aligned}&\vec{J}^s(\vec{R}) = 2\vec{n}\times\vec{H}^i(\vec{R}) + \\ &\sum_{m,n}\frac{\vec{n}\times}{2\pi}\iint_{S_{m,n}}\vec{J}^s(\vec{R}')\times\nabla' g(\vec{R},\vec{R}')ds'\end{aligned} \tag{7-3}$$

Where *m* and *n* are integers numbering the periodic elements, with m=n=0 being the reference element, $S_{m,n}$ is the cone area, and D is periodic distance in x and y direction. k_0 is plane wave propagation constant in free space.

$$\begin{aligned}&k_0 = \omega^2\mu_0\varepsilon_0 \\ &\vec{k}_0 = k_0(\sin\theta\cos\varphi, \sin\theta\sin\varphi, \cos\theta)\end{aligned} \tag{7-4}$$

R' is the position vector of an arbitrary point on cone surface.

Cone profile and TE and TM incidence are indicated in Fig. 7.1

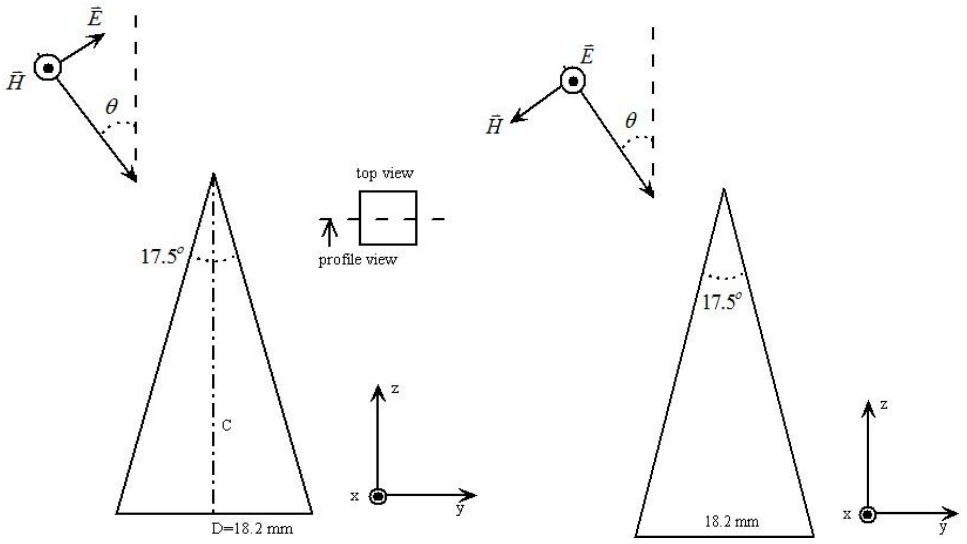

(a) (b)

Fig. 7.1. One cone profile and incidence configuration

(a) TMz incidence (b) TEz incidence.

Surface function of cone is

$$z = f(x,y) = C\left(1 - \frac{2\sqrt{x^2+y^2}}{D}\right) \tag{7-5}$$

where C is the height of cone. Then normal direction on the surface is

$$\vec{n} = \left(-\frac{\partial f(x,y)}{\partial x}, -\frac{\partial f(x,y)}{\partial y}, 1\right) / \sqrt{\left(\frac{\partial f(x,y)}{\partial x}\right)^2 + \left(\frac{\partial f(x,y)}{\partial y}\right)^2 + 1} \tag{7-6}$$

For TM case

$$\vec{n} \times \vec{H}^i(\vec{R}) = \frac{e^{-j\vec{k}_0 \cdot \vec{R}}}{\sqrt{\left(\frac{\partial f(x,y)}{\partial x}\right)^2 + \left(\frac{\partial f(x,y)}{\partial y}\right)^2 + 1}} \left(\hat{x} \cdot 0 + \hat{y} H_0 - \hat{z} H_0 \frac{\partial f(x,y)}{\partial y}\right) \tag{7-7}$$

H_0 is the magnitude of incident wave. The current is just on PEC surface, which leads to

$$\vec{n}' \cdot \vec{J}(\vec{R}') = 0 \qquad \Rightarrow$$
$$\vec{J}_z(\vec{R}') = \frac{\partial f(x', y')}{\partial x'} \vec{J}_x(\vec{R}') + \frac{\partial f(x', y')}{\partial y'} \vec{J}_y(\vec{R}') \tag{7-8}$$

$$dS' = dx'dy' \sqrt{\left(\frac{\partial f(x', y')}{\partial x'} \right)^2 + \left(\frac{\partial f(x', y')}{\partial y'} \right)^2 + 1} \tag{7-9}$$

Plug Equation (7-7), (7-8) and (7-9) into Equation (7-1), and we just consider x and y component,

$$\begin{aligned} &\frac{F_x(R)}{2} + \frac{\partial f(x, y)}{\partial y} \sum_{m,n} \iint_{S_{m,n}} dx'dy' G(\vec{R}, \vec{R}') \\ &\times \left[(x - x') F_y(R') - (y - y') F_x(R') \right] + \sum_{m,n} \iint_{S_{m,n}} dx'dy' G(\vec{R}, \vec{R}') \\ &\times \left(\left\{ -(x - x') \frac{\partial f(x', y')}{\partial x'} + \left[f(x, y) - f(x', y') \right] \right\} \right. \\ &\left. \times F_x(R') - (x - x') \frac{\partial f(x', y')}{\partial y'} F_y(R') \right) = 0 \end{aligned} \tag{7-10}$$

And

$$\begin{aligned} &\frac{F_y(R)}{2} - \frac{\partial f(x, y)}{\partial x} \sum_{m,n} \iint_{S_{m,n}} dx'dy' G(\vec{R}, \vec{R}') \\ &\times \left[(x - x') F_y(R') - (y - y') F_x(R') \right] + \sum_{m,n} \iint_{S_{m,n}} dx'dy' G(\vec{R}, \vec{R}') \\ &\times \left(\left\{ -(y - y') \frac{\partial f(x', y')}{\partial y'} - \left[f(x, y) - f(x', y') \right] \right\} \right. \\ &\left. \times F_y(R') - (y - y') \frac{\partial f(x', y')}{\partial x'} F_x(R') \right) = H_0 e^{-j\vec{k}_0 \cdot \vec{R}} \end{aligned} \tag{7-11}$$

Where $G(R, R')$ is the gradient of Green's function $g(R, R')$

$$G(\vec{R}, \vec{R}') = \nabla' g(\vec{R}, \vec{R}') = \frac{(-jk_0 \left| \vec{R} - \vec{R}' \right| - 1) e^{-jk_0 \left| \vec{R} - \vec{R}' \right|}}{4\pi \left| \vec{R} - \vec{R}' \right|^3} \tag{7-12}$$

The weighted surface current components are defined as

$$\vec{F}_x(\vec{R}) = \vec{J}(\vec{R}) \cdot \hat{x} \sqrt{\left(\frac{\partial f(x,y)}{\partial x}\right)^2 + \left(\frac{\partial f(x,y)}{\partial y}\right)^2 + 1}$$
$$\vec{F}_y(\vec{R}) = \vec{J}(\vec{R}) \cdot \hat{y} \sqrt{\left(\frac{\partial f(x,y)}{\partial x}\right)^2 + \left(\frac{\partial f(x,y)}{\partial y}\right)^2 + 1} \tag{7-13}$$

For TE case

$$\vec{n} \times \vec{H}^i(\vec{R}) = \frac{e^{-j\vec{k}_0 \cdot \vec{R}}}{\sqrt{\left(\frac{\partial f(x,y)}{\partial x}\right)^2 + \left(\frac{\partial f(x,y)}{\partial y}\right)^2 + 1}} \times \left(\hat{x} H_0 \left(\cos\theta - \frac{\partial f(x,y)}{\partial y} \sin\theta \right) + \hat{y} H_0 \frac{\partial f(x,y)}{\partial x} \sin\theta - \hat{z} H_0 \frac{\partial f(x,y)}{\partial x} \cos\theta \right) \tag{7-14}$$

So we can get the full equation for TE case by just changing the right side of Equation (7-10) and (7-11).

$$RHS = H_0 e^{-j\vec{k}_0 \cdot \vec{R}} \left(\cos\theta - \frac{\partial f(x,y)}{\partial y} \sin\theta \right)$$
$$RHS = H_0 e^{-j\vec{k}_0 \cdot \vec{R}} \frac{\partial f(x,y)}{\partial x} \sin\theta \tag{7-15}$$

7.1.2 MFIE in spectral domain

Because of the periodicity and plane wave incidence, these currents must satisfy Floquet's theorem, which is

$$\vec{J}^s(\vec{R} + \hat{x} m D_x + \hat{y} n D_y) = \vec{J}(\vec{R}) e^{-j(k_x D_x m + k_y D_y n)} \tag{7-16}$$

From Appendix B, the vector potential created by a doubly periodic cone array is

$$
\begin{aligned}
\vec{A}(\vec{R}) &= \frac{\mu}{4\pi}\iint_{S_t}\vec{J}(\vec{R}')\frac{e^{-j\vec{k}_0\cdot(\vec{R}-\vec{R}')}}{\left|\vec{R}-\vec{R}'\right|}dS' \\
&= \frac{\mu}{4\pi}\sum_{m,n}\iint_{S}\vec{J}(\vec{R}')\frac{e^{-j\vec{k}_0\cdot(\vec{R}-\vec{R}'-\hat{x}mD_x-\hat{y}nD_y)}}{\left|\vec{R}-\vec{R}'-\hat{x}mD_x-\hat{y}nD_y\right|}dS' \\
&= \begin{cases} \dfrac{\mu}{2jk_0D^2}\displaystyle\sum_{k,l}\iint_{S}\vec{J}(\vec{R}')\frac{e^{-j\vec{k}_+\cdot(\vec{R}-\vec{R}')}}{r_z}dS' & z \geq z' \\ \dfrac{\mu}{2jk_0D^2}\displaystyle\sum_{k,l}\iint_{S}\vec{J}(\vec{R}')\frac{e^{-j\vec{k}_-\cdot(\vec{R}-\vec{R}')}}{r_z}dS' & z < z' \end{cases}
\end{aligned}
\tag{7-17}
$$

Where S is surface area of reference cone and

$$
\begin{aligned}
k_x' &= k_x + \frac{2k\pi}{D_x} \\
k_y' &= k_y + \frac{2l\pi}{D_y} \\
r_z &= \begin{cases} \sqrt{1-\left(\dfrac{k_x'}{k_0}\right)^2-\left(\dfrac{k_y'}{k_0}\right)^2} & \left(\dfrac{k_x'}{k_0}\right)^2+\left(\dfrac{k_y'}{k_0}\right)^2 \leq 1 \\ -j\sqrt{\left(\dfrac{k_x'}{k_0}\right)^2+\left(\dfrac{k_y'}{k_0}\right)^2-1} & \left(\dfrac{k_x'}{k_0}\right)^2+\left(\dfrac{k_y'}{k_0}\right)^2 > 1 \end{cases} \\
\vec{k}_\pm &= \hat{x}k_x' + \hat{y}k_y' \pm \hat{z}k_0r_z = k_0\vec{r}_\pm
\end{aligned}
\tag{7-18}
$$

H field is calculated as

$$
\begin{aligned}
\vec{H}^s(\vec{R}) = \frac{-1}{2D^2}\sum_{k,l}\iint_{S}[&u(z-z')\vec{r}_+\times\vec{J}(\vec{R})\frac{e^{-j\vec{k}_+\cdot(\vec{R}-\vec{R}')}}{r_z} + \\
&u(z'-z)\vec{r}_-\times\vec{J}(\vec{R})\frac{e^{-j\vec{k}_-\cdot(\vec{R}-\vec{R}')}}{r_z}]dS'
\end{aligned}
\tag{7-19}
$$

Where

$$
u(\xi) = \begin{cases} 1 & \xi \geq 0 \\ 0 & \xi < 0 \end{cases}
\tag{7-20}
$$

Origin MFIE is coming from the boundary condition that expresses the total electric current density induced at any point on the surface of PEC

$$\vec{J}(\vec{R}) = \vec{n} \times \left(\vec{H}^i(\vec{R}) + \vec{H}^s(\vec{R}) \right) \tag{7-21}$$

Where H^i and H^s stand for the incident and scattered magnetic field respectively.

Plug (7-19) into (7-21), we get

$$\begin{aligned} &\vec{J}^s(\vec{R}) + \vec{n} \times \left(\frac{1}{2D^2} \sum_{k,l} \iint_S [u(z-z')\vec{r}_+ \times \vec{J}(\vec{R}') \frac{e^{-j\vec{k}_+ \cdot (\vec{R}-\vec{R}')}}{r_z} + \right. \\ &\left. u(z'-z)\vec{r}_- \times \vec{J}(R') \frac{e^{-j\vec{k}_- \cdot (\vec{R}-\vec{R}')}}{r_z}] dS' \right) = \vec{n} \times \vec{H}^i(\vec{R}) \end{aligned} \tag{7-22}$$

We can take $\vec{n} \times$ into quadrature

$$\begin{aligned} \vec{n} \times \vec{r}_+ \times \vec{J}(\vec{R}') &= \hat{x} \left(-\frac{\partial f(x,y)}{\partial y} (r_{+x} J_{y'} - r_{+y} J_{x'}) - (r_{+z} J_{x'} - r_{+x} J_{z'}) \right) \\ &+ \hat{y} \left((r_{+y} J_{z'} - r_{+z} J_{y'}) + \frac{\partial f(x,y)}{\partial x} (r_{+x} J_{y'} - r_{+y} J_{x'}) \right) \\ &+ \hat{z} \left(\frac{\partial f(x,y)}{\partial y} (r_{+y} J_{z'} - r_{+z} J_{y'}) - \frac{\partial f(x,y)}{\partial x}_{x} (r_{+z} J_{x'} - r_{+x} J_{z'}) \right) \end{aligned} \tag{7-23}$$

Plug (7-6), (7-7), (7-8), (7-9) and (7-23) into (7-22) left part, we may get

$$
\begin{aligned}
&LHS \cdot \hat{x} = F_x(\vec{R}) + \frac{1}{2D^2}\sum_{k,l}\iint_S dx'dy' \\
&\left[u(z-z')\frac{e^{-j\vec{k}_+\cdot(\vec{R}-\vec{R}')}}{r_z}\left(\left(\frac{\partial f(x,y)}{\partial y}r_{+y} - r_{+z} + r_{+x}\frac{\partial f(x',y')}{\partial x'}\right)F_x(R')\right.\right. \\
&\left.\left. + \left(-\frac{\partial f(x,y)}{\partial y}r_{+x} + r_{+x}\frac{\partial f(x',y')}{\partial y'}\right)F_y(R')\right)\right] \\
&+ \left[u(z'-z)\frac{e^{-j\vec{k}_-\cdot(\vec{R}-\vec{R}')}}{r_z}\left(\left(\frac{\partial f(x,y)}{\partial y}r_{-y} - r_{-z} + r_{-x}\frac{\partial f(x',y')}{\partial x'}\right)F_x(R')\right.\right. \\
&\left.\left. + \left(-\frac{\partial f(x,y)}{\partial y}r_{-x} + r_{-x}\frac{\partial f(x',y')}{\partial y'}\right)F_y(R')\right)\right]
\end{aligned}
\tag{7-24}
$$

$$
\begin{aligned}
&LHS \cdot \hat{y} = F_y(\vec{R}) + \frac{1}{2D^2}\sum_{k,l}\iint_S dx'dy' \\
&\left[u(z-z')\frac{e^{-j\vec{k}_+\cdot(\vec{R}-\vec{R}')}}{r_z}\left(\left(\frac{\partial f(x',y')}{\partial x'}r_{+y} - \frac{\partial f(x,y)}{\partial x}r_{+y}\right)F_x(R') + \right.\right. \\
&\left.\left. \left(-r_{+z} + r_{+y}\frac{\partial f(x',y')}{\partial y'} + \frac{\partial f(x,y)}{\partial x}r_{+x}\right)F_y(R')\right)\right] \\
&\left[u(z'-z)\frac{e^{-j\vec{k}_-\cdot(\vec{R}-\vec{R}')}}{r_z}\left(\left(\frac{\partial f(x',y')}{\partial x'}r_{-y} - \frac{\partial f(x,y)}{\partial x}r_{-y}\right)F_x(R') + \right.\right. \\
&\left.\left. \left(-r_{-z} + r_{-y}\frac{\partial f(x',y')}{\partial y'} + \frac{\partial f(x,y)}{\partial x}r_{-x}\right)F_y(R')\right)\right]
\end{aligned}
\tag{7-25}
$$

Right part of (7-22) is the same with that in spatial domain formula (7-10) and (7-11).

7.2 Coiflets Implementation in MFIE

7.2.1 Coiflets Implementation in spatial domain MFIE

To solve the coupled integral equations (7-10) and (7-11), we apply the Galerkin based method of moments. First we expand the unknown function $F_x(\vec{R})$ and $F_y(\vec{R})$ in term of Coiflets

$$\begin{aligned} F_x(\vec{R}) &= \sum_i \sum_j \alpha_{i,j} \varphi_{j_0,i}(x) \varphi_{j_0,j}(y) \\ F_y(\vec{R}) &= \sum_i \sum_j \beta_{i,j} \varphi_{j_0,i}(x) \varphi_{j_0,j}(y) \end{aligned} \tag{7-26}$$

Substituting the expansions into the integral equations (7-10), multiplying $\varphi_{j_0,u}(x)\ \ \varphi_{j_0,v}(y)$

And integrating, we arrive at

$$\begin{aligned} &\sum_{ij} \frac{1}{2} \alpha_{ij} \iint dxdy \varphi_{j_0,i}(x) \varphi_{j_0,j}(y) \varphi_{j_0,u}(x) \varphi_{j_0,v}(y) + \\ &\sum_{m,n} \sum_{i,j} \iint \iint dx'dy'dxdy G(\vec{R}, \vec{R}' + \hat{x}mD + \hat{y}nD) \varphi_{j_0,i}(x' + mD) \times \\ &\varphi_{j_0,j}(y' + nD) \varphi_{j_0,u}(x) \varphi_{j_0,v}(y) \Big\{ \alpha_{ij} e^{-j(k_x mD + k_y nD)} \Big[f(x,y) - f(x',y') \\ &-(y - y' - nD) \frac{\partial f(x,y)}{\partial y} - (x - x' - mD) \frac{\partial f(x',y')}{\partial x'} \Big] \\ &+ \beta_{ij} e^{-j(k_x mD + k_y nD)} \left[(x - x' - mD) \frac{\partial f(x,y)}{\partial y} - (x - x' - mD) \frac{\partial f(x',y')}{\partial y'} \right] \Big\} \\ &= 0 \end{aligned} \tag{7-27}$$

Imposing orthogonality and one point quadrature we obtain

$$\frac{1}{2}\alpha_{uv}+\sum_{mn}\sum_{ij}\left(\frac{1}{2^{\frac{j_0}{2}}}\right)^4 G(x_i+mD,y_j+nD;x_u,y_v)\times$$
$$\left\{\alpha_{ij}e^{-j(k_x mD+k_y nD)}\left[f(x_u,y_v)-f(x_i+mD,y_j+nD)-\right.\right.$$
$$\left.(y_v-y_j-nD)\frac{\partial f(x_u,y_v)}{\partial y}-(x_u-x_i-mD)\frac{\partial f(x_i+mD,y_j+nD)}{\partial x}\right] \qquad (7\text{-}28)$$
$$+\beta_{ij}e^{-j(k_x mD+k_y nD)}$$
$$\left.\left[(x_u-x_i-mD)\frac{\partial f(x_u,y_v)}{\partial y}-(x_u-x_i-mD)\frac{\partial f(x_i+mD,y_j+nD)}{\partial y}\right]\right\}$$
$$=0$$

In the same manner, we can discretize the other integral equation in terms of Coiflets coefficients. The matrix form of the discretized MFIE is

$$\left\{\frac{1}{2}I+\begin{bmatrix}Q & R\\ S & T\end{bmatrix}\right\}\begin{bmatrix}\alpha_{uv}\\ \beta_{uv}\end{bmatrix}=\begin{bmatrix}h_{uv}\\ p_{uv}\end{bmatrix} \qquad (7\text{-}29)$$

Where I is the identity matrix and

$$Q_{ij,uv}=\sum_{mn}\left(\frac{1}{2^{\frac{j_0}{2}}}\right)^4 G(x_i+mD,y_j+nD;x_u,y_v)e^{-j(k_x mD+k_y nD)}\times$$
$$\left[f(x_u,y_v)-f(x_i,y_j)-(y_v-y_j-nD)\frac{\partial f(x_u,y_v)}{\partial y}\right.$$
$$\left.-(x_u-x_i-mD)\frac{\partial f(x_i,y_j)}{\partial x}\right]$$
$$R_{ij,uv}=\sum_{mn}\left(\frac{1}{2^{\frac{j_0}{2}}}\right)^4 G(x_i+mD,y_j+nD;x_u,y_v)e^{-j(k_x mD+k_y nD)}\times$$
$$\left[(x_u-x_i-mD)\frac{\partial f(x_u,y_v)}{\partial y}-(x_u-x_i-mD)\frac{\partial f(x_i,y_j)}{\partial y}\right]$$

$$S_{ij,uv} = \sum_{mn} \left(\frac{1}{2^{\frac{j_0}{2}}} \right)^4 G(x_i + mD, y_j + nD; x_u, y_v) e^{-j(k_x mD + k_y nD)} \times$$
$$\left[(y_v - y_j - nD) \frac{\partial f(x_u, y_v)}{\partial x} - (y_v - y_j - nD) \frac{\partial f(x_i, y_j)}{\partial x} \right]$$
$$T_{ij,uv} = \sum_{mn} \left(\frac{1}{2^{\frac{j_0}{2}}} \right)^4 G(x_i + mD, y_j + nD; x_u, y_v) e^{-j(k_x mD + k_y nD)} \times \quad (7\text{-}30)$$
$$\left[f(x_u, y_v) - f(x_i, y_j) - (x_u - x_i - nD) \frac{\partial f(x_u, y_v)}{\partial x} \right.$$
$$\left. -(y_v - y_j - nD) \frac{\partial f(x_i, y_j)}{\partial y} \right]$$

$$h_{uv} = 0$$
$$p_{uv} = \left(\frac{1}{2^{\frac{j_0}{2}}} \right)^2 H_0 e^{-j\bar{k}_0 \cdot (\hat{x} x_u + \hat{y} y_v + \hat{z} f(x_u, y_v))} \quad (7\text{-}31)$$

7.2.2 Coiflets Implementation in spectral domain MFIE

For periodical problem, unknown current on edge is nonzero which limits Coiflets implementation. Since Coiflets can only be utilized when boundary value is zero. So we may consider using Intervallic Coiflets as bases to expand unknown current. However the edge bases will no longer have the property with vanishing moments, which may lead more computation effort. In order avoid this loss, we will expand the unknown current to two periodical current which have zero value at the boundary.

Let us begin with a 1-D problem. For $\cos(2\pi x)$, the period is 1. And we expand it with j0=4 Coiflets as illustrated in Fig. 7.2

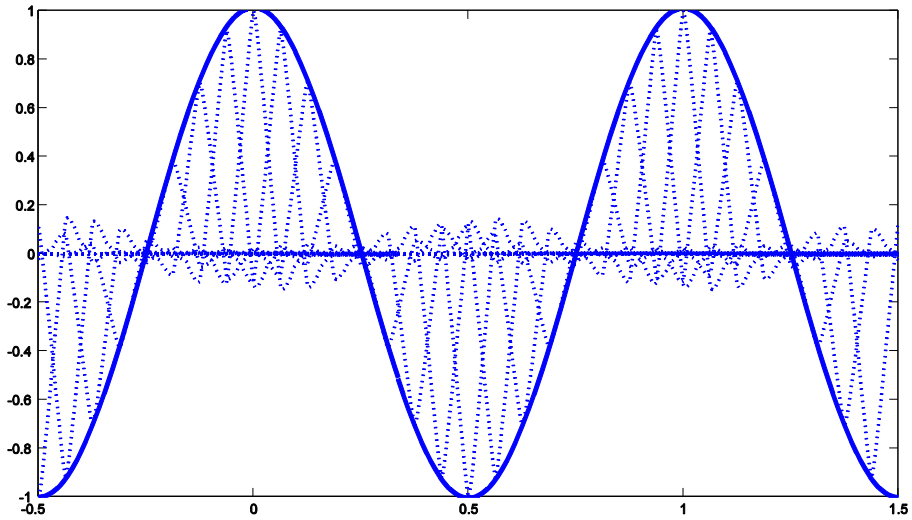

Fig. 7.2. Function $\cos(2\pi x)$ expanded with Coiflets.

For bases center located in one period [0, 1) is

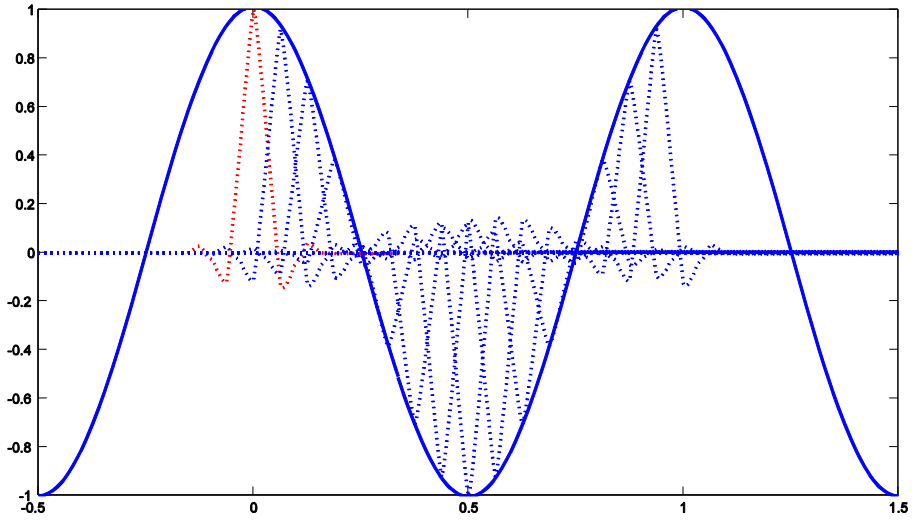

Fig. 7.3. Coiflets with center located in [0, 1).

Fig. 7.4 indicates the summation of these bases multiply with expansion coefficients. If j is big enough, support of these bases will all located in [-0.5, 0.5] which is double of $\cos(2\pi x)$ function period.

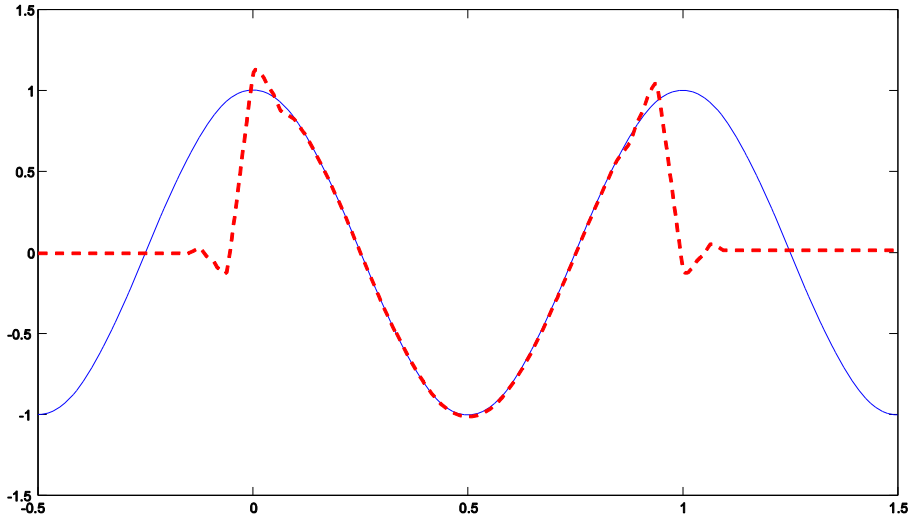

Fig. 7.4. Summation of Coiflets with center located in [0, 1).

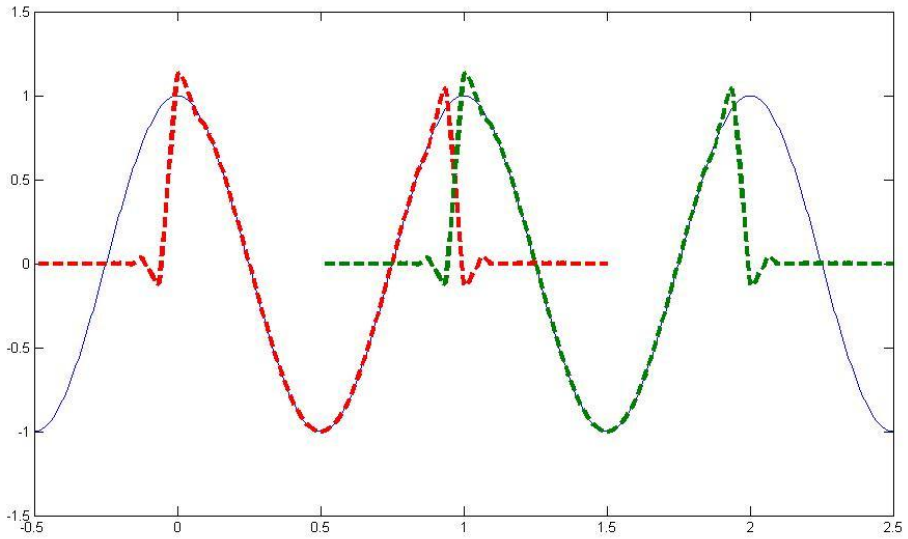

Fig. 7.5. Two new periodical function.

So $\cos(2\pi x)$ function can be expanded to two periodical functions with doubled period and zero value at boundary. We will utilize this idea to our surface current as illustrated in Fig. 7.6, each black box means one cone area projecting to xy plane. There are four shade styles, each of them stand for core part of new double-period current. Red box means the boundary of new double-period current.

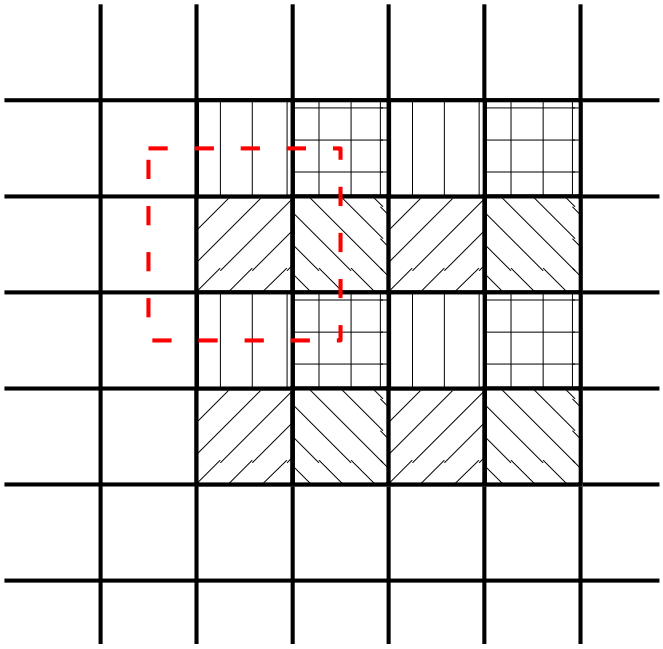

Fig. 7.6. Doubled period surface current.

According to Floquet's theorem (7-16), total surface current is

$$\begin{aligned}
&\vec{J}^s(\vec{R}+\hat{x}D) = \vec{J}(\vec{R})e^{-j(k_xD)} \\
&\vec{J}^s(\vec{R}+\hat{y}D) = \vec{J}(\vec{R})e^{-j(k_yD)} \\
&\vec{J}^s(\vec{R}+\hat{x}D+\hat{y}D) = \vec{J}(\vec{R})e^{-j(k_xD_x+k_yD_y)} \\
&\Rightarrow \\
&total = \sum_{m,n}\vec{J}^s(\vec{R}+\hat{x}2mD+\hat{y}2nD)\times(1+e^{-j(k_xD)}+e^{-j(k_yD)}+e^{-j(k_xD_x+k_yD_y)})
\end{aligned} \tag{7-32}$$

And Plug it into (7-24), and double the period let D=2D, we will arrive at

$$
\begin{aligned}
&F_x(\vec{R}) + \frac{1}{8D^2}\sum_{k,l}\iint_S dx'dy' \\
&\left[u(f(x,y)-f(x',y'))\frac{e^{-j\vec{k}_+\cdot(\vec{R}-\vec{R}')}}{r_z}\left(\left(\frac{\partial f(x,y)}{\partial y}r_{+y} - r_{+z} + r_{+x}\frac{\partial f(x',y')}{\partial x'}\right)F_x(R')\right.\right. \\
&\left.\left.+\left(-\frac{\partial f(x,y)}{\partial y}r_{+x} + r_{+x}\frac{\partial f(x',y')}{\partial y'}\right)F_y(R')\right)B_+\right] \\
&+\left[u(f(x',y')-f(x,y))\frac{e^{-j\vec{k}_-\cdot(\vec{R}-\vec{R}')}}{r_z}\left(\left(\frac{\partial f(x,y)}{\partial y}r_{-y} - r_{-z} + r_{-x}\frac{\partial f(x',y')}{\partial x'}\right)F_x(R')\right.\right. \\
&\left.\left.+\left(-\frac{\partial f(x,y)}{\partial y}r_{-x} + r_{-x}\frac{\partial f(x',y')}{\partial y'}\right)F_y(R')\right)B_-\right] = 0
\end{aligned}
\tag{7-33}
$$

Where

$$
\begin{aligned}
B_+ &= \left(1 + e^{-j(k_x D)}e^{j(k_{+x}D)} + e^{-j(k_y D)}e^{j(k_{+y}D)} + e^{-j(k_x D_x + k_y D_y)}e^{j(k_{+x}D + k_{+y}D)}\right) \\
B_- &= \left(1 + e^{-j(k_x D)}e^{j(k_{-x}D)} + e^{-j(k_y D)}e^{j(k_{-y}D)} + e^{-j(k_x D_x + k_y D_y)}e^{j(k_{-x}D + k_{-y}D)}\right)
\end{aligned}
\tag{7-34}
$$

We will the same thing as we did in 7.2.1. First we expand the unknown function $F_x(\vec{R})$ and $F_y(\vec{R})$ in term of Coiflets just in one new period area.

$$
\begin{aligned}
F_x(\vec{R}) &= \sum_i\sum_j \tilde{\alpha}_{i,j}\varphi_{j_0,i}(x)\varphi_{j_0,j}(y) \\
F_y(\vec{R}) &= \sum_i\sum_j \tilde{\beta}_{i,j}\varphi_{j_0,i}(x)\varphi_{j_0,j}(y)
\end{aligned}
\tag{7-35}
$$

Please note that bases only located in core area. Substituting the expansions into the integral equations (7-33), multiplying $\varphi_{j_0,u}(x)$ $\varphi_{j_0,v}(y)$

And integrating, we arrive at

$$
\begin{aligned}
&\sum_{ij} \tilde{\alpha}_{ij} \iint dxdy \varphi_{j_0,i}(x)\varphi_{j_0,j}(y)\varphi_{j_0,u}(x)\varphi_{j_0,v}(y) + \\
&\frac{1}{8D^2}\sum_{k,l}\sum_{i,j}\iint\iint dx'dy'dxdy \varphi_{j_0,i}(x')\varphi_{j_0,j}(y')\varphi_{j_0,u}(x)\varphi_{j_0,v}(y) \\
&\left[u(f(x,y)-f(x',y'))\frac{e^{-j\vec{k}_+\cdot(\vec{R}-\vec{R}')}}{r_z}\left(\left(\frac{\partial f(x,y)}{\partial y}r_{+y} - r_{+z} + r_{+x}\frac{\partial f(x',y')}{\partial x'}\right)\tilde{\alpha}_{ij}\right.\right. \\
&\left.\left. + \left(-\frac{\partial f(x,y)}{\partial y}r_{+x} + r_{+x}\frac{\partial f(x',y')}{\partial y'}\right)\tilde{\beta}_{ij}\right)B_+\right] \\
&+\left[u(f(x',y')-f(x,y))\frac{e^{-j\vec{k}_-\cdot(\vec{R}-\vec{R}')}}{r_z}\left(\left(\frac{\partial f(x,y)}{\partial y}r_{-y} - r_{-z} + r_{-x}\frac{\partial f(x',y')}{\partial x'}\right)\tilde{\alpha}_{ij}\right.\right. \\
&\left.\left. + \left(-\frac{\partial f(x,y)}{\partial y}r_{-x} + r_{-x}\frac{\partial f(x',y')}{\partial y'}\right)\tilde{\beta}_{ij}\right)B_-\right] \\
&= 0
\end{aligned}
\tag{7-36}
$$

Imposing orthogonality and one point quadrature we obtain

$$
\begin{aligned}
&\tilde{\alpha}_{uv} + \frac{1}{8D^2}\sum_{kl}\sum_{ij}\left(\frac{1}{2^{\frac{j_0}{2}}}\right)^4 \\
&\left[u(f(x_u,y_v)-f(x_i,y_j))\frac{e^{-j\vec{k}_+\cdot(\vec{R}_{uv}-\vec{R}'_{ij})}}{r_z}\left(\left(\frac{\partial f(x_u,y_v)}{\partial y}r_{+y} - r_{+z} + r_{+x}\frac{\partial f(x_i,y_j)}{\partial x}\right)\tilde{\alpha}_{ij}\right.\right. \\
&\left.\left. + \left(-\frac{\partial f(x_u,y_v)}{\partial y}r_{+x} + r_{+x}\frac{\partial f(x_i,y_j)}{\partial y}\right)\tilde{\beta}_{ij}\right)B_+\right] \\
&+\left[u(f(x_i,y_j)-f(x_u,y_v))\frac{e^{-j\vec{k}_-\cdot(\vec{R}_{uv}-\vec{R}'_{ij})}}{r_z}\left(\left(\frac{\partial f(x_u,y_v)}{\partial y}r_{-y} - r_{-z} + r_{-x}\frac{\partial f(x_i,y_j)}{\partial x}\right)\tilde{\alpha}_{ij}\right.\right. \\
&\left.\left. + \left(-\frac{\partial f(x_u,y_v)}{\partial y}r_{-x} + r_{-x}\frac{\partial f(x_i,y_j)}{\partial y}\right)\tilde{\beta}_{ij}\right)B_-\right] \\
&= 0
\end{aligned}
\tag{7-37}
$$

Where

$$
\begin{aligned}
\vec{R}_{uv} &= \hat{x}x_u + \hat{y}y_v + \hat{z}f(x_u,y_v) \\
\vec{R}_{ij} &= \hat{x}x_i + \hat{y}y_j + \hat{z}f(x_i,y_j)
\end{aligned}
\tag{7-38}
$$

In the same manner, we can discretize the other integral equation in terms of Coiflets coefficients. The matrix form of the discretized MFIE is

$$\left\{ I + \begin{bmatrix} \tilde{Q} & \tilde{R} \\ \tilde{S} & \tilde{T} \end{bmatrix} \right\} \begin{bmatrix} \tilde{\alpha}_{uv} \\ \tilde{\beta}_{uv} \end{bmatrix} = \begin{bmatrix} h_{uv} \\ p_{uv} \end{bmatrix} \tag{7-39}$$

Where I is the identity matrix and

$$\tilde{Q}_{ij,uv} = \frac{1}{8D^2} \sum_{kl} \sum_{ij} \left(\frac{1}{2^{\frac{j_0}{2}}} \right)^4$$

$$\left[u(f(x_u, y_v) - f(x_i, y_j)) \frac{e^{-j\vec{k}_+ \cdot (\vec{R}_{uv} - \vec{R}'_{ij})}}{r_z} \left(\frac{\partial f(x_u, y_v)}{\partial y} r_{+y} - r_{+z} + r_{+x} \frac{\partial f(x_i, y_j)}{\partial x} \right) B_+ \right.$$

$$\left. + u(f(x_i, y_j) - f(x_u, y_v)) \frac{e^{-j\vec{k}_- \cdot (\vec{R}_{uv} - \vec{R}'_{ij})}}{r_z} \left(\frac{\partial f(x_u, y_v)}{\partial y} r_{-y} - r_{-z} + r_{-x} \frac{\partial f(x_i, y_j)}{\partial x} \right) B_- \right]$$

$$\tilde{R}_{ij,uv} = \frac{1}{8D^2} \sum_{kl} \sum_{ij} \left(\frac{1}{2^{\frac{j_0}{2}}} \right)^4$$

$$\left[u(f(x_u, y_v) - f(x_i, y_j)) \frac{e^{-j\vec{k}_+ \cdot (\vec{R}_{uv} - \vec{R}'_{ij})}}{r_z} \left(-\frac{\partial f(x_u, y_v)}{\partial y} r_{+x} + r_{+x} \frac{\partial f(x_i, y_j)}{\partial y} \right) B_+ \right.$$

$$\left. + u(f(x_i, y_j) - f(x_u, y_v)) \frac{e^{-j\vec{k}_- \cdot (\vec{R}_{uv} - \vec{R}'_{ij})}}{r_z} \left(\frac{\partial f(x_u, y_v)}{\partial y} r_{-y} - r_{-z} + r_{-x} \frac{\partial f(x_i, y_j)}{\partial x} \right) B_- \right]$$

$$\tilde{S}_{ij,uv} = \frac{1}{8D^2}\sum_{kl}\sum_{ij}\left(\frac{1}{2^{\frac{j_0}{2}}}\right)^4$$

$$\left[u(f(x_u,y_v)-f(x_i,y_j))\frac{e^{-j\vec{k}_+\cdot(\vec{R}_{uv}-\vec{R}'_{ij})}}{r_z}\left(-\frac{\partial f(x_u,y_v)}{\partial x}r_{+y}+r_{+y}\frac{\partial f(x_i,y_j)}{\partial x}\right)B_+\right.$$

$$\left.+u(f(x_i,y_j)-f(x_u,y_v))\frac{e^{-j\vec{k}_-\cdot(\vec{R}_{uv}-\vec{R}'_{ij})}}{r_z}\left(\frac{\partial f(x_u,y_v)}{\partial x}r_{-x}-r_{-z}+r_{-y}\frac{\partial f(x_i,y_j)}{\partial y}\right)B_-\right] \quad (7\text{-}40)$$

$$\tilde{T}_{ij,uv} = \frac{1}{8D^2}\sum_{kl}\sum_{ij}\left(\frac{1}{2^{\frac{j_0}{2}}}\right)^4$$

$$\left[u(f(x_u,y_v)-f(x_i,y_j))\frac{e^{-j\vec{k}_+\cdot(\vec{R}_{uv}-\vec{R}'_{ij})}}{r_z}\left(\frac{\partial f(x_u,y_v)}{\partial x}r_{+x}-r_{+z}+r_{+y}\frac{\partial f(x_i,y_j)}{\partial y}\right)B_+\right.$$

$$\left.+u(f(x_i,y_j)-f(x_u,y_v))\frac{e^{-j\vec{k}_-\cdot(\vec{R}_{uv}-\vec{R}'_{ij})}}{r_z}\left(\frac{\partial f(x_u,y_v)}{\partial x}r_{-x}-r_{-z}+r_{-y}\frac{\partial f(x_i,y_j)}{\partial y}\right)B_-\right]$$

$$h_{uv} = 0$$

$$p_{uv} = \left(\frac{1}{2^{\frac{j_0}{2}}}\right)^2 H_0 e^{-j\vec{k}_0\cdot(\hat{x}x_u+\hat{y}y_v+\hat{z}f(x_u,y_v))} \quad (7\text{-}41)$$

CHAPTER 8

SCATTERING FROM A CALIBRATION TARGET

8.1 Comparison of spatial and spectral equations

Over the previous equations, there are summations for spatial and spectral functions. To clarify, we denote the spatial summation by m, n representing the indices of the (m,n) element, with m=n=0 being the reference element. In the spectral summation, k and l represent the (k,l) mode, with k=l=0 being the incident wave. Ideally, both spatial and spectral summations are from -∞ to ∞. Nevertheless, due to finite computer resources, in numerical computations, we have to truncate the summation at M1 and M2 in (8-1) as small as possible, subject to an accepted precision.

$$\sum_{m=-M1}^{M1}\sum_{n=-M1}^{M1}\sum_{k=-M2}^{M2}\sum_{l=-M2}^{M2} \qquad (8\text{-}1)$$

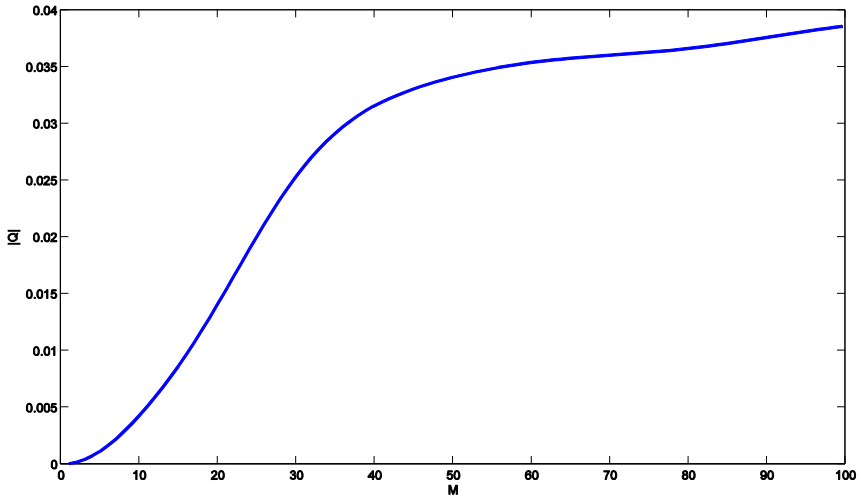

Fig. 8.1. $|\tilde{Q}|$, when receiving and transmitting cell are identical.

Coiflet one-point quadrature may not be accurate enough when the integrand is non-smooth. For both spatial domain and spectral domain integrals, there are singular or non-smooth points. As for spectral domain integration, when the source patch and field patch are at the same elevation, z=z', or they coincide (self-entry in the impedance matrix), we have to subdivide the integration range into many small pieces and sum up the results. From Equations (7-24) (7-25), there are only pure propagation modes, without attenuation when z=z', which leads to underdamped and oscillation behavior. The summations converge slowly and integration for every mode requires a large amount of computation, as indicated in Fig. 8.1. In this situation, spectral domain function is not a good choice, while spatial domain integration may be better off. In fact, numerical integration is needed only if there is an overlap between source and field cells,

and the spatial domain formulation is definitely faster than that of the spectral domain to fill these entries in the impedance matrix. As for spatial domain integration, there is only one cell, m=n=0, needs numerical integration, other m,n value we can still use one-point quadrature property. Let us discuss the numerical integration for m=n=0 case. For this 4-D integration, we will use Gaussian Quadrature for *x* and *y*. Gaussian Quadrature is a weighted sum of function values at specified points x_i and y_i. Then the function will be infinity when $x' = x_i$ $y' = y_i$. As indicated in Fig. 8.2, numerical integration for area close to singular point will be fine pulses, which become coarse when get far away from singular point.

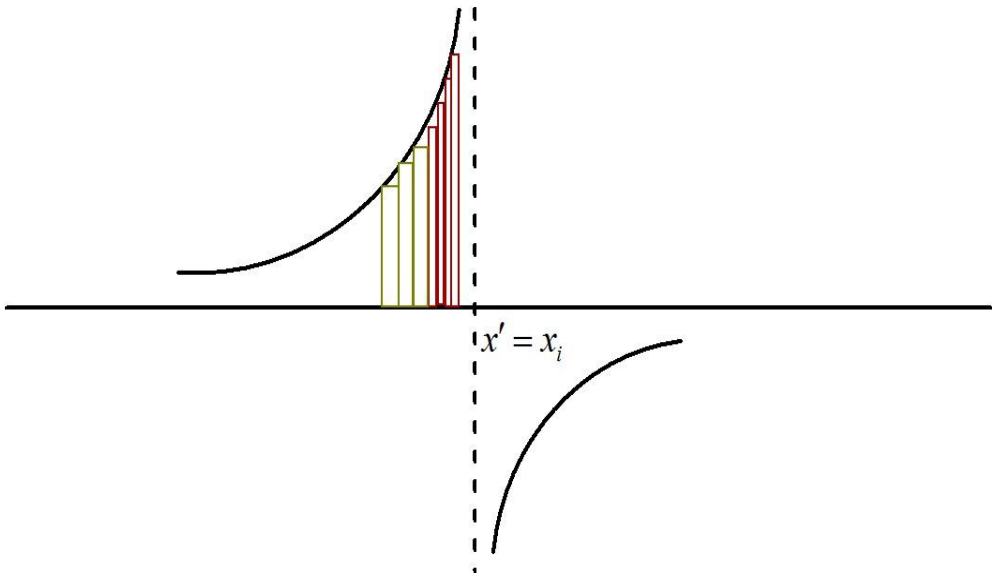

Fig. 8.2. Illustration for numerical integration at singular point.

All parameters for numerical integration, such as number of Gaussian Quadrature sample points, pulse width and etc. are carefully chosen to ensure computation efficiency and precision.

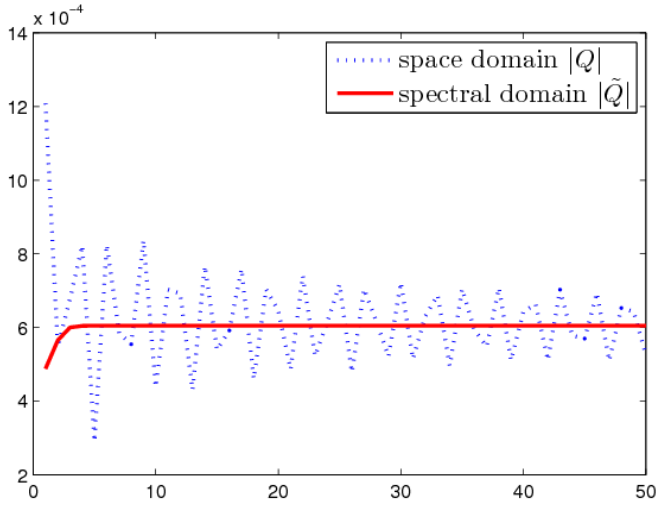

Fig. 8.3. Q and $\tilde{Q}$, when no overlap between source and field cell, the abscissa is the summation range M1 or M2.

On the other hand, when there is no overlap between source and field cells, we may use spectral one-point quadrature property. Fig. 8.3 illustrates the values of Q and $\tilde{Q}$ from the spatial domain equation and spectral domain equation respectively, when the z and z' coordinates of basis center are 0.4D apart. As one can tell, the spectral domain function converges faster than spatial domain function. It just needs 6 modes to get very accurate value. As indicated in (8-2) when k and l are small, the waves are mainly in propagating modes. However,

when k and l become large, wave becomes evanescent with k_{+z} being imaginary. Therefore, computations with spectral domain equations are faster, and we choose spectral domain equations in this situation.

$$\sum_{k,l}\iint_{S}\frac{e^{-j\vec{k}_{+}\cdot(\vec{R}-\vec{R}')}}{r_z}(\cdots)\,dx'dy' \tag{8-2}$$

Computation method for different situation is in Table 4.

Table 4 Impedance Matrix Fill method, where $\rho=\sqrt{(x-x')^2+(y-y')^2}$

situation	**Method of Integration**
$\lvert z-z'\rvert > 0.3D$	One-point + spectral domain
$\lvert z-z'\rvert = 0$ & $\rho = 0$	Numerical Integration for self point One-point + spatial domain for others
$\lvert z-z'\rvert = 0$ & $\rho \neq 0$	One-point + spatial domain
else	4-D Gasussian Quadrature for closest point One-point + spatial domain for others

8.2 Computation result

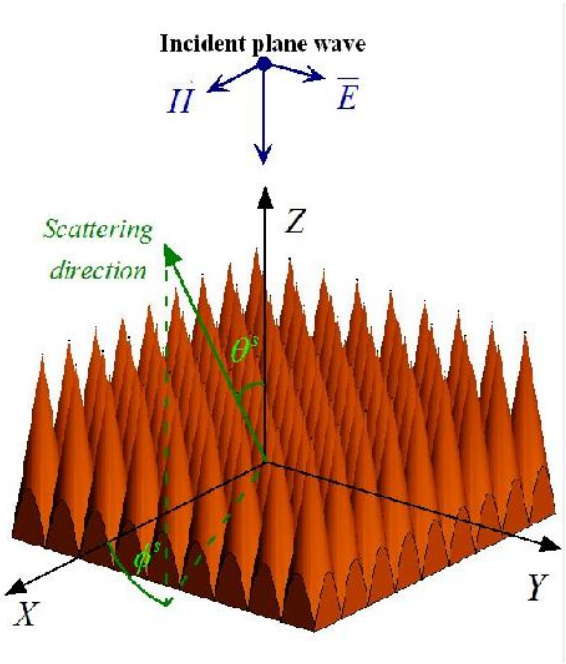

Fig. 8.4. Plane wave incident on 9 by 9 intersected identical PEC cones.

As outlined in the Introduction, once the matrix equation has been solved and the induced surface current on the reference cone is obtained, we calculate the far fields and patterns. By the Floquet theorem, the surface current on each cone in an infinite array is identical, subject to a phase shift. If we analyze the infinite array under a plane wave incidence, the far-zone pattern is a Dirac-δ function similar to $\lim_{n\to\infty} \frac{\sin(nx)}{sinx}$, which seems useless. The current distribution on a finite sized array is obtained as if each cone were among an infinite array. This current distribution is then used to produce the far-zone fields and radar cross sections (RCS). This result is different from the solution of the same finite sized array

illuminated by a tapered wave. Nonetheless, if the array is large enough, the edge effect from the truncation should be relatively small.

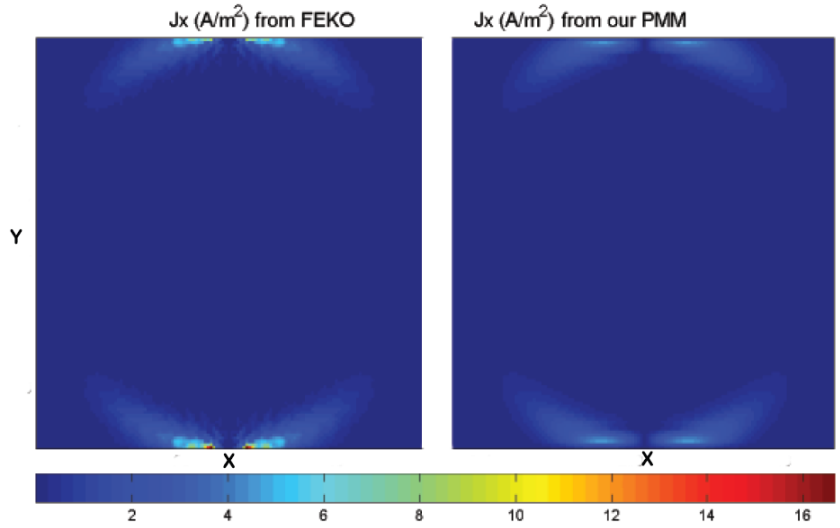

(a)

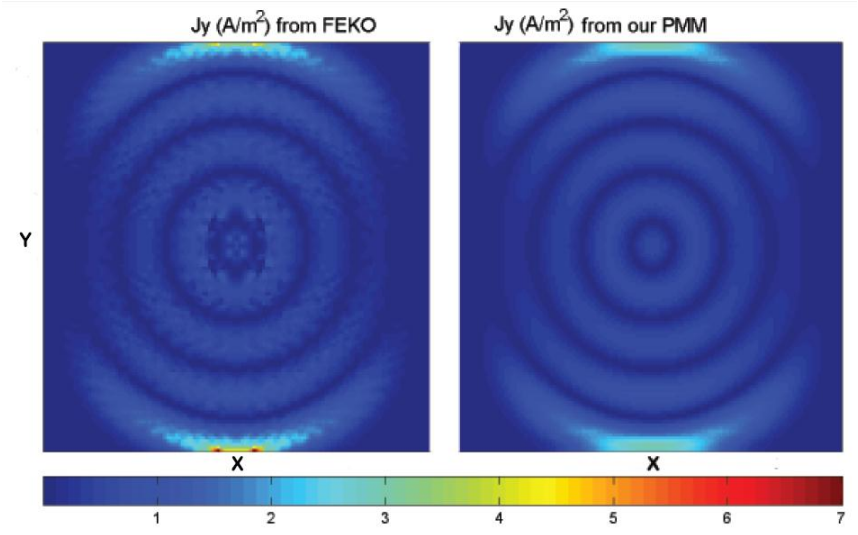

(b)

Fig. 8.5. Surface current on reference cone for normal plane wave incident with H_0=1;

(a) Jx from FEKO and our PMM, (b) Jy from FEKO and our PMM.

Fig. 8.4 configures an array of 9 by 9 identical BEC cones with a normal plane wave incidence. The cone has the period, $D_x = D_y = D = 17.5$mm and vertex angle $\gamma = 17.5^o$. A normally incident plane wave of 10.695 GHz, with $\lambda = 28.03$mm, $\theta_i = 0$, $\phi_i=0$. There are 32×32 Coiflet bases deployed on the reference cone, which makes a total of 2048 unknown surface currents. In order to increase computation efficiency, parallel computation is implemented when fill impedance matrix. The developed parallel algorithm is based on C++ with MPI [28] and run on Saguaro cluster at Arizona State University.

Fig. 8.5 and Fig. 8.6 demonstrate the surface current and bi-static radar cross sections (RCS) of the configuration in Fig. 8.4. The results by our method are compared with the solutions from a RWG-MLFMA based commercial software, FEKO. There are 3751 unknown RWG triangle edges in reference cone for FEKO. As indicated in Fig. 8.5 and Fig. 8.6, there are some differences between peak current at the edges, but RCS are well matched with that from the FEKO.

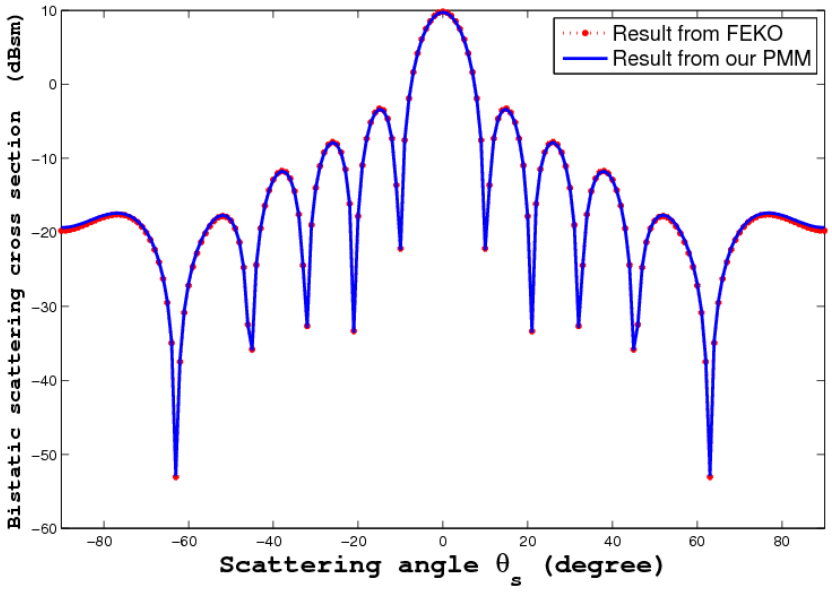
Result from FEKO
Result from our PMM
Bistatic scattering cross section (dBsm)
Scattering angle θs (degree)
10
0
−10
−20
−30
−40
−50
−60
−80
−60
−40
−20
0
20
40
60
80

(a)

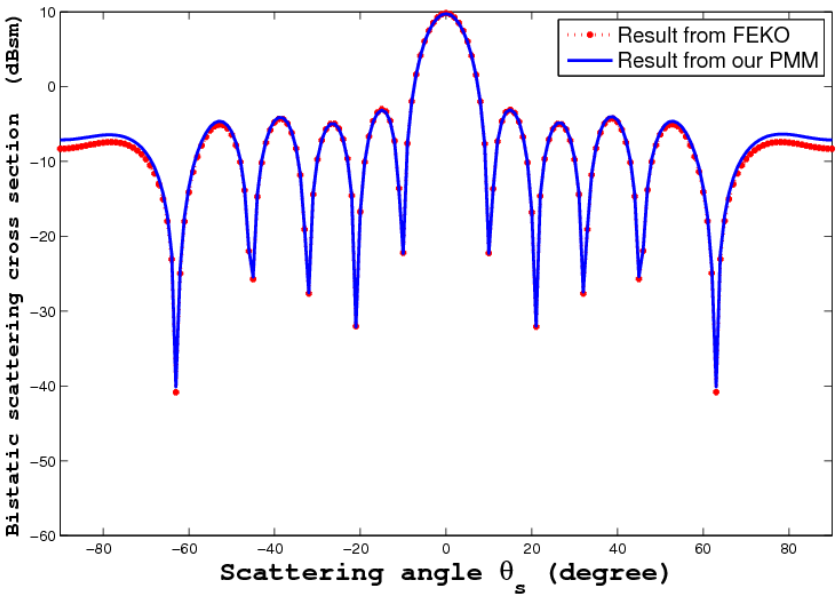
Result from FEKO
Result from our PMM
Bistatic scattering cross section (dBsm)
Scattering angle θs (degree)
10
0
−10
−20
−30
−40
−50
−60
−80
−60
−40
−20
0
20
40
60
80

(b)

Fig. 8.6. Bi-static RCS of 9×9 cone array;

(a) for $\phi_s = 0^o$, (b) for $\phi_s = 90^o$.

The results are compared against that of an RWG-MLFMA based commercial software, FEKO with excellent agreement.

CHAPTER 9

CONCLUSION

9.1 Summary for DGBA

The diffracted Gaussian beam approach is a good method for large scale multi-reflector antenna simulation. Independence of expanded Gaussian beams makes this method much more efficient when the MPI is used on the computers.

9.2 Summary for periodic MoM

Employing the well-posted MFIE, we conducted a full wave analysis for doubly periodically PEC conic array. The proposed algorithm combines the Floquet theorem and Coifman wavelets to perform Galerkin's procedure with high precision and great computational efficiency. Majority entries of the impedance matrix are obtained by Coiflet one-point quadrature. Both spectral domain and spatial domain formulations are derived and used to evaluate the singular or oscillatory entries of impedance matrix, depending on different situations. This hybrid filling process is faster than either the pure spectral PMM or spatial PMM. The results are compared against that of an RWG-MLFMA based commercial software, FEKO with excellent agreement.

REFERENCES

[1] C. Rieckmann, M.R. Rayner, C.G. Parini, D.H. Martin and R.S. Donnan, "Novel modular approach based on Gaussian beam diffraction for analysing quasi-optical multi-reflector antennas", IEE Proc.-Microw. Antennas Propag., vol 149, 3, pp.160-167, June 2002.

[2] DAUBECHIES, I, "The wavelet transform, time-frequency localization and signal analysis", IEEE Trans. Inf. Theory, vol. 36, 5, pp. 961-1005.

[3] EINZIGER, P.D., RAZ, S., and SHAPIRA, M., "Gabor representation and aperture theory", J. Opt. Soc. Am. A, Opt. Image Sci., 3(4), pp. 508-521, 1986.

[4] DESCHAMPS, G.A., "Ray techniques in electromagnetic", Proc. IEEE, 60(9), pp. 1022-1035, 1972.

[5] K. Miyamoto and E. Wolf, "Generalization of the Maggi-Rubinowicz theory of the boundary diffraction wave-Part I", J. Opt. Soc. Am., 52, pp. 615-625, 1962.

[6] K. Miyamoto and E. Wolf, "Generalization of the Maggi-Rubinowicz theory of the boundary diffraction wave-Part II", J. Opt. Soc. Am., 52, pp. 626-637, 1962.

[7] G. Otis, "Application of the boundary-diffraction-wave theory to Gaussian beams", J. Opt. Soc. Am., 64, pp. 1545-1550, 1974.

[8] Takenaka, T., and Fukumitsu, O., "Asymptotic representation of the boundary-diffraction wave for a three-dimensional Gaussian beam incident upon a Kirchhoff half-screen", J. Opt. Soc. Am., , 72, (3), pp. 331-336, 1982.

[9] Amnon Yariv, Pochi Yeh, Photonics, "optical electronics in modern communications", Oxford, 2007.

[10] Leopold B. Felsen, Nathan Marcuvitz, "Radiation and Scattering of Waves", IEEE PRESS, 1994.

[11] Constantine A. Balanis, “Advanced Engineering Electromagnetics”, John Wiley & Sons, 1989.

[12] GRASP8 reflector analysis code user manual, TICRA, Copenhagen, Denmark.

[13] F. T. Ulaby, R. K. Moore, A. K.Fung, “Microwave Remote Sensing,” Addison-Wesley Publishing Company, 1981.

[14] J. T. McLean, A. McCulloch, and E. I. Mohr, “Calibration source for remote sensors,” NASA Special Pub., no. 379, pp. 783-796, 1975.

[15] D. F. Heath, “Large aperture spectral radiance calibration source for ultraviolet remote sensing instruments,” Proc. SPIE, no. 4891, pp. 335-342, 2002.

[16] Junhong Wang, Jungang Miao, Yujie Yang, and Yunmei Chen, “Scattering Property and Emissivity of a Periodic Pyramid Array Covered With Absorbing Material,” IEEE Trans. Antennas Propagat., vol. 56, no. 8, pp. 2656-2663, Aug. 2008.

[17] J. Wang, Y. Yang, J. Miao, and Y. Chen, “Emissivity Calculation for a Finite Circular Array of Pyramidal Absorbers Based on Kirchhoff’s Law of Thermal Radiation,” IEEE Trans. Antennas Propagat., vol. 58, no. 4, pp. 1173-1180, Apr. 2010.

[18] R. Harrington, Field Computation by the Moment Method, IEEE Press, 1996.

[19] Chang-Fa Yang, Walter D. Burnside, and Roger C. Rudduck, “A Periodic Moment Method Solution for TM Scattering from Lossy Dielectric Bodies with Application to Wedge Absorber,” IEEE Trans. Antennas Propagat., vol. 40, no. 6, pp. 652-660, Jun. 1992.

[20] R. Collin, Field Theory of Guided Waves, IEEE Press, 1996.

[21] Chang-Fa Yang, Walter D. Burnside, and Roger C. Rudduck, “A Doubly Periodic Moment Method Solution for the Analysis and Design of an

Absorber Covered Wall," IEEE Trans. Antennas Propagat., vol. 41, no. 5, pp. 600-609, May. 1993.

[22] George W. Pan, "Wavelets in Electromagnetics and Device Modeling," Wiley, 2002.

[23] George W. Pan, Ke Wang, and Douglas, "Coifman Wavelets in 3-D Scattering From Very Rough Random Surfaces," IEEE Trans. Antennas Propagat., vol. 52, no. 11, pp. 3096-3103, Nov. 2004.

[24] G. Pan, M. Toupikov and B. Gilbert, "On the Use of Coifman Intervallic Wavelets in the Method of Moments for Fast Construction of Wavelet Sparsified Matrices," IEEE Trans. AP, vol. 47, no. 7, pp. 1189-1200, July 1999.

[25] A. Cohen, I. Daubechies, and P. Vial, "Wavelets on the interval and fast wavelet transform," Appl. Comput. Harmon. Anal., I, 54-81, 1993.

[26] L. Andersson, N. Hall, B. Jawerth, and G. Peters, "Wavelets on closed subsets of the real line," in Topics in the Theory and Applications of Wavelets, L. Schumaker and G. Webb, Eds., Academic Press, New York, 1994.

[27] Constantine A. Balanis, "Advanced Engineering Electromagnetics," Wiley, 1989.

[28] Gropp, Lusk and Skjellum, Using MPI, MIT Press.

[29] B. A. Munk and G. A. Burrell, "Plane-wave expansion for arrays of arbitrarily oriented piecewise linear elements and its application in determining the impedance of a single linear antenna in a lossy half-space," IEEE Trans. Antennas Propagat., vol. 27, pp. 331-343, May. 1979.

[30] J. H. Richmond, "Radiation and scattering by thin-wire structures in a homogeneous conducting medium," IEEE Trans. Antennas Propagat., vol. Ap-22, pp. 365, Mar. 1974.

Abramowitz Milton and Stegun Irene A., “Handbook of Mathematical Functions (with Formulas, Graphs, and Mathematical Tables),” Dover, 1972.

APPENDIX A

SCHMIDT-CRAMER ORTHOGONALIZATION

For a set of linearly independent basis $\{a_1, a_2, \dots, a_n\}$, we can generate a set of orthonormal bases $\{b_1, b_2, \dots, b_n\}$ as follows:

$$
\begin{aligned}
b_1 &= a_1 \\
b_2 &= a_2 - \frac{\langle a_2, b_1 \rangle}{\langle b_1, b_1 \rangle} b_1 \\
&\cdots \\
b_{k+1} &= a_{k+1} - \frac{\langle a_{k+1}, b_1 \rangle}{\langle b_1, b_1 \rangle} b_1 - \cdots - \frac{\langle a_{k+1}, b_k \rangle}{\langle b_k, b_k \rangle} b_k
\end{aligned}
\qquad \text{(A 1)}
$$

APPENDIX B

THE FIELD FROM AN ARRAY

In this appendix we determine the exact field of an infinite array of dipoles of length *dl* and oriented along the arbitrary unit vector $\hat{p}$ [29]. The double periodical array is located in the XY-plane with inter-element spacing D_x and D_y and the reference element at (0, 0, 0).

The total vector potential $d\vec{A}(x,y,z)$ for an infinite array of dipoles is obtained by simple addition of the vector potentials $d\vec{A}_{qm}$ of each element:

$$d\vec{A}(x,y,z) = \sum_{n=-\infty}^{\infty}\sum_{m=-\infty}^{\infty} d\vec{A}_{qm} = \hat{p}\frac{\mu dl}{4\pi}\sum_{n=-\infty}^{\infty}\sum_{m=-\infty}^{\infty} I_{nm}\frac{e^{-\gamma R_{nm}}}{R_{nm}} \qquad \text{(B 1)}$$

Where $\gamma = \alpha + j\beta$ is the propagation constant in the lossy medium, and

$$R_{nm}{}^2 = a^2 + (mD_y - y)^2 \qquad \text{(B 2)}$$

Where

$$a^2 = (nD_x - x)^2 + z^2 \qquad \text{(B 3)}$$

For an incident plane wave propagating in the direction $\hat{s}$. According to Floquet's theorem (7-16), (B 1) will yield

$$d\vec{A}(x,y,z) = \sum_{n=-\infty}^{\infty} e^{-j\beta n D_x s_x} d\vec{A}_n \qquad \text{(B 4)}$$

Where

$$d\vec{A}_n = \hat{p}\frac{\mu I dl}{4\pi}\sum_{m=-\infty}^{\infty} e^{-j\beta m D_y s_y}\frac{e^{-\gamma R_{nm}}}{R_{nm}} \qquad \text{(B 5)}$$

Simply denotes the vector potential for a single column.

We shall first evaluate $d\vec{A}_n$ by transforming the infinite series in (B 5) into a faster converging series by use of Poisson's sum formula:

$$\sum_{m=-\infty}^{\infty} e^{jm\omega_0 t}F(m\omega_0) = T\sum_{l=-\infty}^{\infty} f(t+lT) \qquad \text{(B 6)}$$

Where $F(\omega)$ is the Fourier transform of $f(t)$, and

$$T = \frac{2\pi}{\omega_0} \qquad \text{(B 7)}$$

From Bateman [30] we obtain the Fourier transform pair:

$$\frac{e^{-\gamma\sqrt{a^2+(\omega-\omega_1)^2}}}{\sqrt{a^2+(\omega-\omega_1)^2}} = \mathbb{F}\left[\frac{e^{j\omega_1 t}}{2j}H_0^{(2)}(a\sqrt{-\gamma^2-t^2})\right] \qquad \text{(B 8)}$$

Comparison of (B 5) and (B 6) and application of (B 2), (B 7) and (B 8) now suggests that we put

$$\omega_0 = D_y, \quad T = \frac{2\pi}{\omega_0} = \frac{2\pi}{D_y}, \quad t = -\beta s_y, \quad \omega_1 = y \qquad \text{(B 9)}$$

By application of Poisson's sum formula (B 6) we then transform (B 5) into

$$d\vec{A}_n = \hat{p}\frac{\mu I dl}{4jD_y}\sum_{l=-\infty}^{\infty} e^{-j\beta y(s_y + l(\lambda/D_y))}H_0^{(2)}(\beta r_\rho\,'a) \qquad \text{(B 10)}$$

where

$$r_\rho' = \sqrt{\left(\frac{\gamma}{j\beta}\right)^2 - \left(s_y + l\frac{\lambda}{D_y}\right)} \qquad \text{(B 11)}$$

Substituting (B 10) into (B 4),

$$d\vec{A} = \hat{p}\frac{\mu I dl}{4jD_y}\sum_{l=-\infty}^{\infty} e^{-j\beta y(s_y + l(\lambda/D_y))} \bullet \sum_{n=-\infty}^{\infty} e^{-j\beta n s_x D_x} H_0^{(2)}(\beta r_\rho' a) \qquad \text{(B 12)}$$

The summation over q in (B 12) is now to be transformed into a faster convergent series by the use of Poisson sum formula similarly as above. We the obtain

$$d\vec{A} = \hat{p}\frac{\mu I dl}{2\gamma D_x D_y}\sum_{k=-\infty}^{\infty}\sum_{l=-\infty}^{\infty}\frac{e^{-\gamma \vec{R}\bullet\hat{r}_\pm}}{r_z}, \qquad for \quad z > or < 0 \qquad \text{(B 13)}$$

Where $\hat{r}_\pm$ and r_z are given by (7-18)

Having determined the vector potential $d\vec{A}$ from the entire array of dipoles as given by (B 13), it is a simple matter to find the magnetic and electric fields from

$$\begin{aligned} d\vec{H}(x,y,z) &= \frac{1}{\mu}\nabla\times\left[d\vec{A}(x,y,z)\right] \\ \vec{E} &= \frac{1}{j\omega\varepsilon}\nabla\times\vec{H} \end{aligned} \qquad \text{(B 14)}$$

Yielding

$$d\vec{H}(x,y,z) = \frac{Idl}{2D_x D_y}\sum_{k=-\infty}^{\infty}\sum_{l=-\infty}^{\infty}\frac{e^{-\gamma\vec{R}\bullet\hat{r}_\pm}}{r_z}\hat{p}\times\hat{r}_\pm \qquad for \quad z > or < 0 \qquad \text{(B 15)}$$

$$d\vec{E}(x,y,z) = \frac{Z_c Idl}{2D_x D_y}\sum_{k=-\infty}^{\infty}\sum_{l=-\infty}^{\infty}\frac{e^{-\gamma\vec{R}\bullet\hat{r}_\pm}}{r_z}[\hat{p}\times\hat{r}_\pm]\times\hat{r}_\pm \qquad for \quad z > or < 0 \qquad \text{(B 16)}$$

APPENDIX C

GAUSSIAN QUADRATURE

Gaussian quadrature 0 is an approximation of the definite integral of a function, stated as a weighted sum of function values at specified points within the domain of integration. An n-point 1D Gaussian is stated as

$$\int_a^b f(x)dx \approx \frac{b-a}{2}\sum_{i=1}^{n}\omega_i f\left(\frac{b-a}{2}x_i + \frac{b+a}{2}\right) \qquad \text{(C 1)}$$

Where x_i is i-th root of P_n, P_n is Legendre polynomials. It weight ω_i is given by

$$\omega_i = \frac{2}{(1-x_i^2)\left[P_n'(x_i)\right]^2} \qquad \text{(C 2)}$$

APPENDIX D

INTEGRAL ALONG THE STEEPEST DESCENT PATH

The integration variable of the integral along SDP in Equation (4-25) is changed from y0 to ζ as follows:

$$\zeta^2 = i\left[d\left(y_s\right) - d\left(y_0\right)\right] \tag{D 1}$$

The SDP transforms into the real axis of the complex ζ plane. The saddle point and poles $y_0=y_s$, y_p^1,y_p^2 correspond to $\zeta=0$, ζ_p, $-\zeta_p$, respectively, where

$$\zeta_p = \left\{i\left[d\left(y_s\right) - d\left(y_p^1\right)\right]\right\}^{1/2} \tag{D 2}$$

The square root is defined so that ζ_p is positive real at $x=x_s$. On substitution of Equation (D1) into (4-25), the integral along SDP becomes

$$\int_{SDP} G\left(y_0\right)\exp\left[ikd\left(y_0\right)\right] = \exp\left[ikd\left(y_s\right)\right]\int_{-\infty}^{\infty} F\left(\zeta\right)\exp\left(-k\zeta^2\right)d\zeta \tag{D 3}$$

Where

$$F\left(\zeta\right) = G\left(y_0\right)\frac{dy_0}{d\zeta} \tag{D 4}$$

In order to take into account the effect of two poles $\zeta=\pm\zeta_p$ on the saddle point $\zeta=0$, we set

$$F(\zeta) = \frac{\kappa}{\zeta - \zeta_p} - \frac{\kappa}{\zeta + \zeta_p} + H(\zeta) \qquad \text{(D 5)}$$

Where $H(\zeta)$ is regular. Approximation of $H(\zeta)$ by $H(0)$ and use of the integral formula

$$\int_{-\infty}^{\infty} \frac{e^{-\Omega\xi^2}}{\xi^2 - \alpha^2} d\xi = \mp i \frac{\pi}{\alpha} erfc\left(\pm i\alpha\sqrt{\Omega}\right) e^{-\Omega\alpha^2} \quad (\mathrm{Im}\,\alpha \lessgtr 0) \qquad \text{(D 6)}$$

Yield the asymptotic representation of the integral along SDP, which is given by Equation (4-27)